

A thermo-elasto-viscoplastic constitutive model for polymers

Joakim Johnsen^{a,*}, Arild Holm Clausen^a, Frode Grytten^b, Ahmed Benallal^c, Odd Sture Hopperstad^a

^a*Structural Impact Laboratory (SIMLab), Department of Structural Engineering, NTNU, Norwegian University of Science and Technology, NO-7491 Trondheim, Norway*

^b*SINTEF Industry, Department of Materials and Nanotechnology, PB 124 Blindern, NO-0314 Oslo, Norway*

^c*LMT, ENS Paris-Saclay/CNRS/Université Paris-Saclay, 61 Avenue du Président Wilson, Cachan Cedex, F 94235, France*

Abstract

In this study, a thermo-elasto-viscoplastic model is developed for a low density cross-linked polyethylene (XLPE) in an attempt to describe the combined effects of temperature and strain rate on the stress-strain response and the self-heating of the material at elevated strain rates. The proposed model consists of two parts. On the one side, Part A models the thermo-elastic and thermo-viscoplastic response, and incorporates an elastic Hencky spring in series with two Ree-Eyring dashpots. The two Ree-Eyring dashpots represent the effects of the main α relaxation and the secondary β relaxation processes on the plastic flow. Part B, on the other side, consists of an eight chain spring capturing the entropic strain hardening due to alignment of the polymer chains during deformation.

The constitutive model was implemented in a nonlinear finite element (FE) code using a semi-implicit stress update algorithm combined with sub-stepping and a numerical scheme to calculate the consistent tangent operator. After calibration to available experimental data, FE simulations with the constitutive model are shown to successfully describe the stress-strain curves, the volumetric strain, the local strain rate and the self-heating observed in the tensile tests. In addition, the FE simulations adequately predict the global response of the tensile tests, such as the force-displacement curves and the deformed shape of the tensile specimen.

Keywords: Temperature, Constitutive model, Polyethylene, XLPE, Strain rate sensitivity, Self-heating

1. Introduction

2 The use of polymers in structural applications has increased during the last decades. Some examples are
3 shock absorbers in cars designed for pedestrian protection, thermal insulation of pipelines in the offshore

*Corresponding author

Email address: joakim.johnsen@ntnu.no (Joakim Johnsen)

4 oil industry and electrical insulation of high-voltage cables. The mechanical behaviour of polymers is com-
5 plex and factors such as strain rate, temperature and stress triaxiality have a great impact on the structural
6 behaviour of polymer components. Thus, it is a challenging task to obtain accurate numerical predictions
7 of the mechanical response of polymeric materials under different loading scenarios. Prototype testing has
8 therefore become a normal way to qualify materials and structural components for given applications in the
9 industry. Qualifying materials in this manner is both costly and time consuming; thus there is a need for
10 sufficiently accurate and easy-to-use material models. By using reliable material models, a limited set of ex-
11 periments can be conducted for calibration purposes, and subsequently, numerical analyses of the structural
12 component can be used either to optimize geometry or to investigate the effect of using different materials.

13 There is a number of available material models for polymers. Haward and Thackray [1] were the first
14 to decouple the stress into one part where the elastic response was modelled by Hookean elasticity and
15 a single Eyring dashpot [2] was employed to represent the inelastic flow, and a second part concerning
16 entropic strain hardening using a Langevin spring derived from non-Gaussian chain statistics [3]. This
17 model was extended to a three-dimensional (3D) formulation by Boyce et al. [4], who also incorporated
18 strain softening and pressure sensitivity. Further development of the entropic strain hardening was done by
19 Arruda et al. [5], resulting in the well-known eight chain model used in the current study. Regarding the
20 flow process, Ree and Eyring [6] extended the original model by Eyring [2] to include several relaxation
21 processes, which in our work are restricted to two, namely the main α relaxation and the secondary β
22 relaxation [7, 8].

23 An important aspect regarding the Ree-Eyring flow process is that it does not include strain hardening.
24 A common way of including strain hardening has been to introduce a backstress, see e.g. [1, 4, 9, 10]. A
25 problem that may arise from this approach is that self-heating, due to the viscous flow, can be underesti-
26 mated. This leads to difficulties when trying to describe thermal softening in polymers at elevated strain
27 rates [11–13]. Another way of including strain hardening was proposed by Hoy and Robbins [14]. Using a
28 multiplicative rate sensitivity formulation where the hardening modulus was scaled by the flow stress, they
29 obtained good results for the strain rates and temperatures covered in their study. However, investigating
30 different polymers at strain rates yielding isothermal conditions, Govaert et al. [15] showed that the mod-
31 elling approach of Hoy and Robbins [14] did not work in general. Instead they suggested to introduce a
32 backstress in addition to viscous strain hardening, where the viscous strain hardening may either be mod-
33 elled by stress-scaling of the hardening modulus [14], or by introducing a non-constant strain dependent

34 activation volume in the Eyring model as proposed by Wendlandt et al. [16]. The latter approach is thor-
35 oughly evaluated by Senden et al. [17]. Their work shows the problematic behaviour in cyclic loading if
36 the entire strain hardening is incorporated in the strain dependent activation volume (or strain dependent
37 reference strain rate), namely that instead of continuing strain hardening when going from tension to com-
38 pression, the model will predict strain softening since the activation volume will start to decrease when the
39 loading direction is reversed. To avoid this unphysical behaviour, a portion of the strain hardening has to be
40 modelled by an inelastic backstress.

41 The viscous behaviour contributes to self-heating in a material. In the studies performed by Adams
42 and Farris [18] and Boyce et al. [19], it was found that about 50 – 80% of the total mechanical work
43 was converted into heat in glassy polymers. On the other hand, studying a semi-crystalline high density
44 polyethylene (HDPE), Hillmansen et al. [20, 21] observed that almost the entire mechanical work was
45 converted into heat. A similar observation was also done by Johnsen et al. [11] on a cross-linked low
46 density polyethylene (XLPE). Since heating of the polymer material will introduce thermal softening, it is
47 evident that a correct prediction of heat generation during deformation is crucial in order for the constitutive
48 model to capture the material behaviour over a range of strain rates. Consequently, taking thermomechanical
49 coupling into account is important in this situation, and in particular accounting for heat conduction within
50 the material and heat convection to the surroundings. There are many examples of thermomechanically
51 coupled constitutive models. Arruda et al. [13] and Boyce et al. [19] combined an elastic Hookean response
52 with non-Newtonian viscous flow and kinematic hardening based on the alignment of the polymer chains.
53 Adopting a similar approach, Richeton et al. [22] presented a model able to span the glass transition
54 temperature. More recent developments were made by Garcia-Gonzalez et al. [23] who extended the
55 isothermal model proposed by Polanco-Loria et al. [24] to include thermomechanical coupling. This model
56 combines an elastic Neo-Hookean response with rate-dependent yielding and plastic flow governed by the
57 Raghava yield function [25] and kinematic hardening modelled by an eight chain spring. Another extension
58 of the Polanco-Loria et al. [24] model was done by Ognedal et al. [26], who added isotropic hardening
59 of the Raghava yield surface. Anand et al. [27] and Ames et al. [28] presented a thermomechanically
60 coupled constitutive model describing the large deformation behaviour of amorphous polymers, including
61 loading/unloading and torsion. In another study, Maurel-Pantel et al. [29] proposed a visco-hyperelastic
62 constitutive model to capture large deformations and self-heating in a semi-crystalline polyamide 66. In
63 the study by Srivastava et al. [30], the model presented by Anand et al. [27] was extended to span the

64 glass transition temperature. The material model's ability to span the glass transition temperature is of
65 course desirable, but it inevitably introduces additional parameters and adds complexity to the calibration
66 procedure. Thus, we have chosen to limit our study to temperatures above the glass transition, namely the
67 leathery region [8] between the glass transition and melting temperatures.

68 The thermomechanical behaviour of a cross-linked low density polyethylene (XLPE) material was stud-
69 ied experimentally in Johnsen et al. [11] using the experimental set-up described in Johnsen et al. [31].
70 Similar studies concerned with the effect of low temperatures on the mechanical behaviour have been per-
71 formed, see e.g. Richeton et al. [32], Brown et al. [33], Serban et al. [34] and Bauwens-Crowet [35].
72 All of these studies revealed the same trends as observed by Johnsen et al. [11], namely that lowering the
73 temperature increases the yield stress in a similar manner as an increase in strain rate, indicating that the
74 yield stress may be determined from thermal activation theory [6, 36]. However, in these studies [32–35] the
75 strains were obtained by mechanical measurement techniques, as opposed to the local measurements made
76 possible by digital image correlation (DIC) in Johnsen et al. [11]. Further, self-heating due to elevated
77 strain rates was not reported [32–35].

78 In this article, based on the experimental investigation outlined above and described in the next sec-
79 tion, we present a thermo-elasto-viscoplastic model to describe the thermomechanical behaviour of XLPE
80 at different temperatures and strain rates. The proposed model has two parts: Part A consists of an hyper-
81 elastic Hencky spring in series with two Ree-Eyring dashpots. The two Ree-Eyring dashpots model the
82 effects of the main α relaxation and the secondary β relaxation processes on the plastic flow. Part B con-
83 sists of an entropic eight chain spring modelling strain hardening due to alignment of the polymer chains
84 during deformation. The constitutive model is implemented in the commercial finite element (FE) pro-
85 gram Abaqus/Standard as a UMAT subroutine. A semi-implicit stress update algorithm is combined with a
86 sub-stepping procedure to ensure convergence. The consistent tangent operator is found by numerical differ-
87 entiation as proposed by Miehe [37] and Sun et al. [38]. This paper is organized as follows: first, we briefly
88 describe the material investigated here along with the main experimental results obtained in [11]. Then the
89 constitutive model is presented within a general thermodynamical framework including the heat equation
90 used to calculate the temperature increase. This is followed by a brief outline of the numerical integration
91 algorithm and the calibration procedure. Finally, the results obtained from simulations are compared to the
92 experimental findings allowing some concluding remarks to be drawn.

2. Material, experimental set-up, methods and experimental results

In this study, we consider the material behaviour of a cross-linked low density polyethylene (XLPE) material. The material is produced by Borealis under the product name Borlink LS4201S [39] and was received from Nexans Norway as extruded high-voltage cable segments where the copper conductor had been removed. The dimensions of the cable segments were $128 \text{ mm} \times 73 \text{ mm} \times 22.5 \text{ mm}$ (length \times diameter \times thickness). Material properties of the XLPE material are given in Table 1.

Table 1: Material properties for the XLPE material. All parameters are given for room temperature [11, 31].

Density, ρ_0 (kg/m^3)	Specific heat capacity, C_v ($\text{J}/(\text{kg}\cdot\text{K})$)	Thermal conductivity, k ($\text{W}/(\text{m}\cdot\text{K})$)	Heat transfer coefficient to air, h_c ($\text{W}/(\text{m}^2\cdot\text{K})$)	Thermal expansion coefficient, α (K^{-1})
922	3546	0.56	21	$2 \cdot 10^{-4}$ [40]

Uniaxial tension and compression tests were performed at four temperatures ($T = -30 \text{ }^\circ\text{C}$, $T = -15 \text{ }^\circ\text{C}$, $T = 0 \text{ }^\circ\text{C}$ and $T = 25 \text{ }^\circ\text{C}$) and three different cross-head velocities ($v = 0.04 \text{ mm/s}$, $v = 0.4 \text{ mm/s}$ and $v = 4.0 \text{ mm/s}$). Assuming that all deformation happens over the parallel section of the tensile specimen, these cross-head velocities correspond to initial nominal strain rates $\dot{\epsilon}$ of 0.01 s^{-1} , 0.1 s^{-1} and 1.0 s^{-1} . A detailed description of the experimental set-up can be found in Johnsen et al. [31]. Figure 1 shows the cylindrical specimens used in the tension experiments.

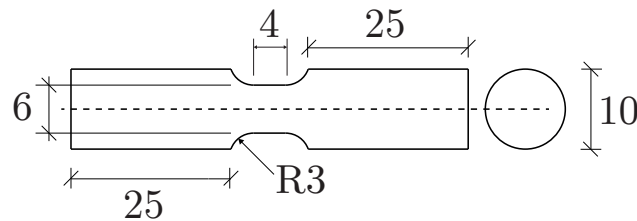


Figure 1: Illustration of the tensile test specimen. All measures are in mm.

A condensed illustration of the local stress-strain behaviour reported in [11] is given in Figure 2. It appears that temperature-time equivalence applies for the XLPE material, namely that a decrease in temperature has a similar impact on Young's modulus and the flow stress as an increase in strain rate. Using two Ree-Eyring [6] dashpots, Johnsen et al. [11] successfully described the flow stress as a function of both temperature and strain rate, while they used a phenomenological expression similar to that proposed by Arruda et al. [13] to describe the temperature dependence of Young's modulus. It is also noted from Figure 2 that the locking stretch, defined as the stretch where an abrupt change in strain hardening occurs,

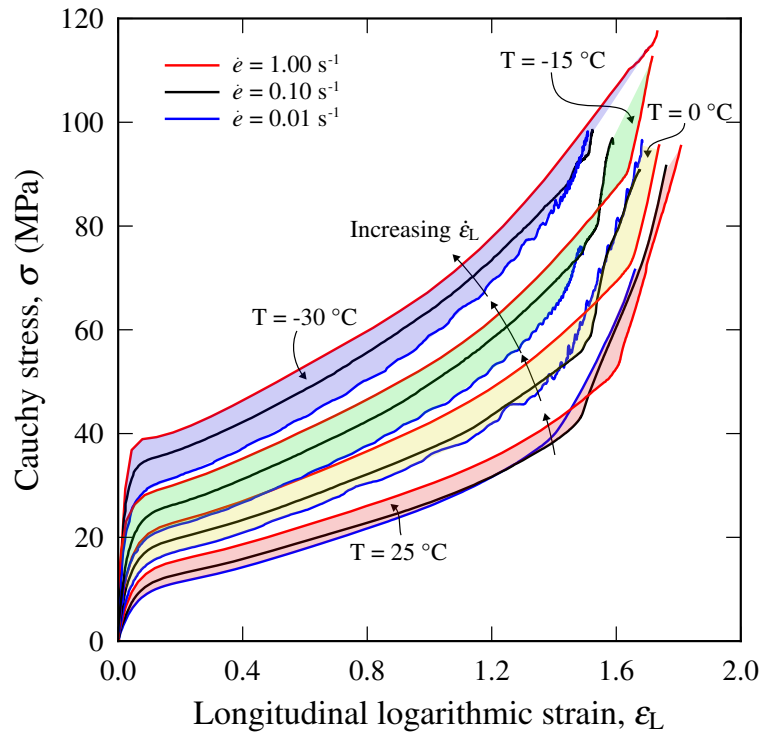


Figure 2: Condensed version of all stress-strain curves from experiments showing how the material behaviour is affected by changing the temperature and the strain rate. Adapted from Johnsen et al. [11].

112 increases with increasing strain rate. This phenomenon is believed to be caused by increased chain mobility
 113 due to self-heating at elevated strain rates. The material was also found to be close to incompressible at
 114 room temperature, while it is moderately compressible at the three lower temperatures. In terms of self-
 115 heating, it was shown in [11] that the lowest strain rate ($\dot{\epsilon} = 0.01 \text{ s}^{-1}$) gave close to isothermal conditions.
 116 At the intermediate strain rate ($\dot{\epsilon} = 0.1 \text{ s}^{-1}$) self-heating was observed, but due to the duration of the test,
 117 heat conduction inside the material and heat convection to the surroundings caused the temperature to de-
 118 crease at the end of the experiment. For the tests performed at the highest strain rate ($\dot{\epsilon} = 1.0 \text{ s}^{-1}$), close
 119 to adiabatic conditions were met, resulting in a temperature increase in the material between 20 °C and 35
 120 °C. Further, uniaxial compression tests revealed that the yield stress is similar in tension and compression.
 121 The test results from [11] will be shown in full together with predictions from the numerical simulations in
 122 Section 6.

123 A more detailed presentation and discussion of the experimental set-up, the methods used to extract local
 124 stress-strain data and self-heating from experiments, and the experimental results, are found in Johnsen et
 125 al. [11, 31].

126 **3. Constitutive model**

127 In this section we present the thermo-elasto-viscoplastic model proposed to describe the thermomechanical behaviour observed in the experiments on the XLPE material. In addition to the features addressed in 128 Figure 2, the model also aims at capturing the volumetric response and self-heating. The model has been 129 implemented in the implicit framework provided by Abaqus/Standard as a user subroutine (UMAT). 130

131 *3.1. Overview*

132 As seen from the kinematics in Figure 3a, we use a multiplicative split of the deformation gradient tensor 133 \mathbf{F} to separate between elastic and plastic deformation [41]. Applying the plastic deformation gradient \mathbf{F}^p an 134 undeformed material element is mapped from the reference configuration (Ω_0) to the elastically unloaded 135 intermediate configuration ($\tilde{\Omega}$). Finally, compatibility is obtained by mapping the material element from $\tilde{\Omega}$ 136 to the current configuration (Ω) via the elastic deformation gradient \mathbf{F}^e , viz.

$$\mathbf{F} = \mathbf{F}^e \mathbf{F}^p \quad (1)$$

137 Our material model, see Figure 3b, has two contributions: Part A (intermolecular) describes the hyperelastic 138 and viscoplastic behaviour, while Part B represents the orientational hardening due to the alignment of the 139 polymer network. From Figure 3b it follows that the deformation gradient is equal in the two parts, viz.

$$\mathbf{F} = \mathbf{F}_A = \mathbf{F}_A^e \mathbf{F}_A^p = \mathbf{F}_B \quad (2)$$

140 where subscripts A and B denote Parts A and B of the rheological model, respectively. Polar decomposition 141 of the elastic and plastic parts of the deformation gradient of Part A yields

$$\mathbf{F}_A^e = \mathbf{V}_A^e \mathbf{R}_A^e = \mathbf{R}_A^e \mathbf{U}_A^e \quad (3)$$

$$\mathbf{F}_A^p = \mathbf{V}_A^p \mathbf{R}_A^p = \mathbf{R}_A^p \mathbf{U}_A^p \quad (4)$$

142 where \mathbf{R} is the rotation tensor, \mathbf{U} and \mathbf{V} are the right and left stretch tensors, respectively, and superscripts 143 e and p denote the elastic and plastic parts. The isochoric deformation gradient tensor $\bar{\mathbf{F}}$ is defined by

$$\bar{\mathbf{F}} = J^{-1/3} \mathbf{F} \quad (5)$$

144 where $J = \det(\mathbf{F})$ is the Jacobian determinant, thus implying that $\det(\bar{\mathbf{F}}) = 1$. The isochoric left Cauchy- 145 Green deformation tensor $\bar{\mathbf{B}}$ and the isochoric left stretch tensor $\bar{\mathbf{V}}$ are defined as

$$\bar{\mathbf{B}} = \bar{\mathbf{F}} \bar{\mathbf{F}}^T = J^{-2/3} \mathbf{F} \mathbf{F}^T = J^{-2/3} \mathbf{B} \quad (6)$$

$$\bar{\mathbf{V}} = \sqrt{\bar{\mathbf{B}}} = J^{-1/3} \sqrt{\mathbf{B}} = J^{-1/3} \mathbf{V} \quad (7)$$

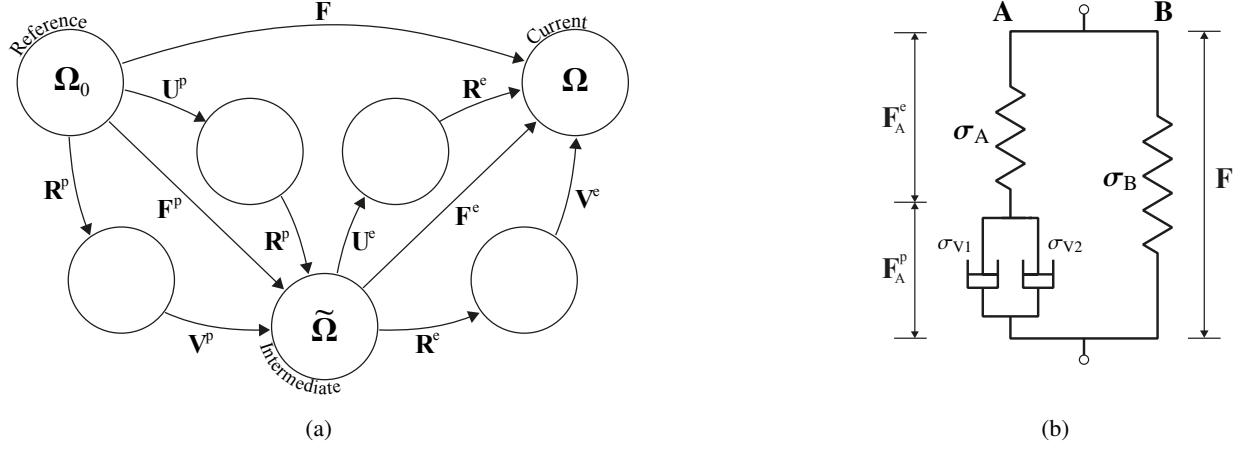


Figure 3: Large deformations kinematics using a multiplicative split of the deformation gradient, \mathbf{F} , is shown in (a), and (b) shows the rheological model.

146 where $\mathbf{B} = \mathbf{F}\mathbf{F}^T$ is the left Cauchy-Green deformation tensor. Throughout this study the plastic deformation
 147 is assumed to be isochoric, i.e., $J_A^p = 1$ and thus $J_A^e = J$ since the decomposition of the Jacobian determinant
 148 reads $J = \det(\mathbf{F}) = \det(\mathbf{F}_A^e) \det(\mathbf{F}_A^p) = J_A^e J_A^p$. With respect to the elastic and plastic parts of the deformation
 149 gradient tensor, we then obtain the following relations:

$$\bar{\mathbf{F}}_A^e = J^{-1/3} \mathbf{F}_A^e, \quad \bar{\mathbf{B}}_A^e = \bar{\mathbf{F}}_A^e (\bar{\mathbf{F}}_A^e)^T = J^{-2/3} \mathbf{B}_A^e, \quad \bar{\mathbf{V}}_A^e = J^{-1/3} \mathbf{V}_A^e \quad (8)$$

$$\bar{\mathbf{F}}_A^p = \mathbf{F}_A^p, \quad \bar{\mathbf{B}}_A^p = \mathbf{F}_A^p (\mathbf{F}_A^p)^T = \mathbf{B}_A^p, \quad \bar{\mathbf{V}}_A^p = \mathbf{V}_A^p \quad (9)$$

150 According to the rheological model in Figure 3b, the free energy is decomposed as follows

$$\psi = \psi_A + \psi_B \quad (10)$$

151 where ψ_A and ψ_B are the free energies of Parts A and B, respectively. Note that the free energy function is
 152 here defined per unit reference mass. In the same manner, the Cauchy stress tensor is decomposed as

$$\boldsymbol{\sigma} = \boldsymbol{\sigma}_A + \boldsymbol{\sigma}_B \quad (11)$$

153 where $\boldsymbol{\sigma}_A$ and $\boldsymbol{\sigma}_B$ are the Cauchy stress tensors acting in Parts A and B of the rheological model.

154 3.1.1. Part A - Intermolecular

155 Both the elastic and viscoplastic responses of Part A are taken to be isochoric. The elastic response is
 156 defined by the Hencky free energy [42], i.e.,

$$\rho_0 \psi_A = \mu_A(\theta) \text{tr} \left[\left(\ln(\bar{\mathbf{V}}_A^e) \right)^2 \right] \quad (12)$$

157 where ρ_0 is the initial density of the material and θ is the absolute temperature. The shear modulus of the
 158 elastic spring is temperature dependent through the following expression

$$\mu_A(\theta) = \mu_{A,\text{ref}} \exp[-a_A (\theta - \theta_{\text{ref}})] \quad (13)$$

159 where θ_{ref} is a reference temperature, $\mu_{A,\text{ref}}$ is the shear modulus at the reference temperature, and a_A is a
 160 parameter governing the temperature sensitivity.

161 The Kirchhoff stress tensor $\boldsymbol{\tau}_A$ is obtained from the free energy function in Equation (12) as [43]

$$\boldsymbol{\tau}_A = 2\rho_0 \frac{\partial \psi_A}{\partial \mathbf{B}_A^e} \mathbf{B}_A^e = \rho_0 \frac{\partial \psi_A}{\partial \ln(\mathbf{V}_A^e)} = 2\mu_A(\theta) \ln(\bar{\mathbf{V}}_A^e) \quad (14)$$

162 The above derivation is not trivial and a detailed derivation can be found in [42]. It then follows that the
 163 Cauchy stress tensor $\boldsymbol{\sigma}_A$ is given as

$$\boldsymbol{\sigma}_A = \frac{1}{J} \boldsymbol{\tau}_A \quad (15)$$

164 Now we focus on the thermo-viscoplastic part of the constitutive model. Since the yield stress in ten-
 165 sion and compression was found to be approximately the same [11], the pressure-insensitive von Mises
 166 equivalent stress is used

$$\sigma_D^{\text{vm}} = \sqrt{\frac{3}{2} \boldsymbol{\sigma}'_D : \boldsymbol{\sigma}'_D} \quad (16)$$

167 where $\boldsymbol{\sigma}'_D = \boldsymbol{\sigma}_D - \frac{1}{3} \text{tr}(\boldsymbol{\sigma}_D) \mathbf{1}$ is the deviatoric part of the driving stress $\boldsymbol{\sigma}_D = \boldsymbol{\sigma}_A$. From the rheological
 168 model (Figure 3b) it is evident that the equivalent driving stress must be balanced by the viscous stress σ_V
 169 associated with the Ree-Eyring [6] dashpots. Thus, assuming that the contribution from each dashpot is
 170 additive [7], we obtain

$$\sigma_V = \sigma_{V1} + \sigma_{V2} = \sum_{x=\alpha,\beta} \frac{k_B \theta}{V_x} \text{arsinh} \left(\frac{\dot{p}}{\dot{p}_{0,x}^*} \exp \left[\frac{\Delta H_x}{R\theta} \right] \right) = \sigma_D^{\text{vm}} \quad (17)$$

171 where α and β denote the contributions from the main and secondary relaxation processes, respectively,
 172 k_B is Boltzmann's constant, V_x is the activation volume, \dot{p} is the equivalent plastic strain rate, ΔH_x is the
 173 activation enthalpy, and R is the universal gas constant. Further, $\dot{p}_{0,x}^*$ is the deformation dependent reference
 174 equivalent plastic strain rates given by

$$\dot{p}_{0,x}^* = \dot{p}_{0,x} \exp \left(-\sqrt{\frac{2}{3}} b_x \|\ln(\mathbf{V}_A^p)\|_2 \right) \quad \text{for } x = \alpha, \beta \quad (18)$$

175 where $\dot{p}_{0,x}$ are the values of $\dot{p}_{0,x}^*$ in the plastically undeformed state in which $\mathbf{V}_A^p = \mathbf{1}$, b_α and b_β are the
 176 parameters governing the deformation dependence, and $\|\ln(\mathbf{V}^p)\|_2$ is the Frobenius norm of the Hencky
 177 strain tensor.

178 The velocity gradient \mathbf{L}_A and its decompositions are given by

$$\mathbf{L}_A = \dot{\mathbf{F}}_A \mathbf{F}_A^{-1} = [\dot{\mathbf{F}}_A^e \mathbf{F}_A^p + \mathbf{F}_A^e \dot{\mathbf{F}}_A^p] (\mathbf{F}_A^p)^{-1} (\mathbf{F}_A^e)^{-1} \quad (19)$$

$$\mathbf{L}_A = \dot{\mathbf{F}}_A^e (\mathbf{F}_A^e)^{-1} + \mathbf{F}_A^e \dot{\mathbf{F}}_A^p \mathbf{F}_A^{-1} = \mathbf{L}_A^e + \mathbf{L}_A^p \quad (20)$$

$$\mathbf{L}_A = \mathbf{D}_A^e + \mathbf{W}_A^e + \mathbf{D}_A^p + \mathbf{W}_A^p \quad (21)$$

179 where \mathbf{D} and \mathbf{W} are in turn the rate-of-deformation tensor and the spin tensor. Due to isotropy, the plastic
 180 spin in the intermediate configuration $\tilde{\mathbf{W}}_A^p$ is taken to be zero [44, 45]. Another consequence of material
 181 isotropy is that the Mandel stress tensor in the intermediate configuration becomes symmetric. This in
 182 combination with an isotropic plastic potential results in a spin-free plastic velocity gradient, i.e. $\mathbf{W}_A^p = \mathbf{0}$
 183 [46]. The plastic rate-of-deformation tensor is given by the flow rule as

$$\mathbf{D}_A^p = \mathbf{L}_A^p = \lambda \frac{\partial g(\boldsymbol{\sigma}_D)}{\partial \boldsymbol{\sigma}_D} \quad (22)$$

184 where λ is a plastic multiplier and $g(\boldsymbol{\sigma}_D)$ is the plastic potential. Assuming that the plastic flow is isochoric,
 185 the plastic potential is taken as

$$g(\boldsymbol{\sigma}_D) = \sqrt{\frac{3}{2} \boldsymbol{\sigma}'_D : \boldsymbol{\sigma}'_D} = \sigma_D^{\text{vm}} \geq 0 \quad (23)$$

186 where the direction of plastic flow \mathbf{N} is obtained from the gradient of the plastic potential,

$$\mathbf{N} = \frac{\partial g(\boldsymbol{\sigma}_D)}{\partial \boldsymbol{\sigma}_D} = \frac{3}{2} \frac{\boldsymbol{\sigma}'_D}{g(\boldsymbol{\sigma}_D)} \quad (24)$$

187 Equivalence in terms of plastic power yields the relation between the equivalent plastic strain rate, \dot{p} , and
 188 the plastic multiplier, λ , viz.

$$\sigma_D^{\text{vm}} \dot{p} = \boldsymbol{\sigma}_D : \mathbf{D}_A^p \Rightarrow \dot{p} = \lambda \quad (25)$$

189 Combining Equations (20) and (22) and inserting $\lambda = \dot{p}$, we obtain the expression for the evolution of the
 190 plastic deformation gradient, i.e.,

$$\dot{\mathbf{F}}_A^p = \dot{p} (\mathbf{F}_A^e)^{-1} \frac{\partial g(\boldsymbol{\sigma}_D)}{\partial \boldsymbol{\sigma}_D} \mathbf{F}_A \quad (26)$$

191 3.1.2. Part B - Orientational hardening

192 The orientational hardening of the material due to the alignment of the polymer chains is captured by
 193 the eight chain model [5]. Following Miehe [47] we define a modified entropic free energy function, viz.

$$\rho_0 \psi_B = \frac{\kappa(\theta)}{2} (\ln(J))^2 - 3\kappa(\theta)\alpha \ln(J)(\theta - \theta_0) + \rho_0 \psi_T(\theta) + \mu_B(\theta) \lambda_{\text{lock}}^2 \left[\left(\frac{\bar{\lambda}_c}{\lambda_{\text{lock}}} \right) \xi + \ln \left(\frac{\xi}{\sinh \xi} \right) \right] \quad (27)$$

194 The shear modulus of Part B is interpreted as a rubbery modulus, i.e.,

$$\mu_B(\theta) = nk_B\theta = \mu_{B,\text{ref}} \frac{\theta}{\theta_{\text{ref}}} \quad (28)$$

195 where n is the chain density, k_B is Boltzmann's constant, and $\mu_{B,\text{ref}}$ is the shear modulus at the reference
 196 temperature. In this study the reference temperature is set equal to 298.15 K, while the initial temperature
 197 is equal to the temperatures at which the experiments were conducted. The bulk modulus $\kappa(\theta)$ could be
 198 temperature dependent as found by Anand [48], but is taken to be constant in this study, i.e.

$$\kappa(\theta) = \kappa_B. \quad (29)$$

199 The linear thermal expansion coefficient α is assumed to be independent of temperature. Further, λ_{lock} is
 200 the locking stretch, $\bar{\lambda}_c = \sqrt{\text{tr}(\bar{\mathbf{B}})}/3$ is an average chain stretch, and

$$\xi = \mathcal{L}^{-1}\left(\frac{\bar{\lambda}_c}{\lambda_{\text{lock}}}\right) \quad (30)$$

201 where \mathcal{L}^{-1} is the inverse Langevin function ($\mathcal{L}(x) = 1/x - \coth x$) approximated by the formula proposed
 202 by Jedynek [49]:

$$\mathcal{L}^{-1}(x) \approx x \frac{3 - 2.6x + 0.7x^2}{(1-x)(1+0.1x)} \quad (31)$$

203 The purely thermal contribution to the free energy, which, assuming that the specific heat capacity is tem-
 204 perature independent, $C_v(\theta) \approx C_v$, is given as [47, 48]

$$\psi_T(\theta) = C_v \left[(\theta - \theta_0) - \theta \ln\left(\frac{\theta}{\theta_0}\right) \right] \quad (32)$$

205 where θ_0 is the initial absolute temperature.

206 The Kirchhoff stress tensor, $\boldsymbol{\tau}_B$, is found after some algebra as [48]

$$\boldsymbol{\tau}_B = 2\rho_0 \frac{\partial \psi_B}{\partial \mathbf{B}} \mathbf{B} = \frac{\mu_B(\theta)\lambda_{\text{lock}}}{3\bar{\lambda}_c} \mathcal{L}^{-1}\left(\frac{\bar{\lambda}_c}{\lambda_{\text{lock}}}\right) \bar{\mathbf{B}}' + \kappa_B \ln(J)\mathbf{1} - 3\kappa_B\alpha(\theta - \theta_0)\mathbf{1} \quad (33)$$

207 where $\mathbf{1}$ is the second order identity tensor and $\bar{\mathbf{B}}' = \bar{\mathbf{B}} - \frac{1}{3}\text{tr}(\bar{\mathbf{B}})\mathbf{1}$ is the deviatoric part of $\bar{\mathbf{B}}$. The Cauchy
 208 stress reads as

$$\boldsymbol{\sigma}_B = \frac{1}{J} \boldsymbol{\tau}_B \quad (34)$$

209 Note that the compressibility has been included entirely in Part B of the rheological model. This was done
 210 to improve the model's description of self-heating, as will be demonstrated in the following section.

211 *3.1.3. Self-heating and dissipation*

212 The internal energy u , defined per unit reference mass, is given in terms of the free energy ψ and the
213 entropy $s \equiv -\partial\psi/\partial\theta$ as

$$u = \psi + \theta s \quad (35)$$

214 Local energy balance is expressed as

$$\rho_0 \dot{u} = \boldsymbol{\tau} : \mathbf{D} + r - \text{div}(\mathbf{q}) \quad (36)$$

215 where r is external heat sources and \mathbf{q} is the heat flux. The deformation power per unit reference volume is
216 decomposed according to

$$\boldsymbol{\tau} : \mathbf{D} = \boldsymbol{\tau}_A : (\mathbf{D}_A^e + \mathbf{D}_A^p) + \boldsymbol{\tau}_B : \mathbf{D} = \boldsymbol{\tau}_A : \mathbf{D}_A^e + \boldsymbol{\tau}_D : \mathbf{D}_A^p + \boldsymbol{\tau}_B : \mathbf{D} \quad (37)$$

217 where $\boldsymbol{\tau}_D = J\boldsymbol{\sigma}_D$, and only the deformation power in the two dashpots contributes to the intrinsic dissipation.
218 After some calculations, the rates of change of the free energy and the entropy are obtained as [47]

$$\rho_0 \dot{\psi} = \boldsymbol{\tau}_A : \mathbf{D}_A^e + \boldsymbol{\tau}_B : \mathbf{D} - \rho_0 \dot{\theta} s \quad (38)$$

$$\rho_0 \theta \dot{s} = -\theta \frac{\partial \boldsymbol{\tau}_A}{\partial \theta} : \mathbf{D}_A^e - \theta \frac{\partial \boldsymbol{\tau}_B}{\partial \theta} : \mathbf{D} + \rho_0 \bar{C}_v \dot{\theta} \quad (39)$$

219 where the specific heat capacity \bar{C}_v is given by

$$\bar{C}_v = \theta \frac{\partial s}{\partial \theta} = C_v - \frac{1}{\rho_0} \theta a_A^2 \mu(\theta) \text{tr} \left[\left(\ln(\bar{\mathbf{V}}_A^e) \right)^2 \right] \quad (40)$$

220 Note that beside temperature, this specific heat capacity is also dependent on deformation. Furthermore,

$$\frac{\partial \boldsymbol{\tau}_A}{\partial \theta} = -2a_A \mu_A(\theta) \ln(\bar{\mathbf{V}}_A^e) = -a_A \boldsymbol{\tau}_A \quad (41)$$

$$\theta \frac{\partial \boldsymbol{\tau}_B}{\partial \theta} = \boldsymbol{\tau}_B - \kappa_B [\ln(J) + 3\alpha\theta_0] \mathbf{1} \quad (42)$$

221 The dissipation inequality may be stated as [43]

$$\mathcal{D} \equiv -\rho_0 (\dot{\psi} + s\dot{\theta}) + \boldsymbol{\tau} : \mathbf{D} - \frac{\mathbf{q}}{\theta} \cdot \frac{\partial \theta}{\partial \mathbf{x}} \geq 0 \quad (43)$$

222 where \mathbf{x} is the position vector in the current configuration. Inserting Equations (37) and (38) yields

$$\mathcal{D} = \boldsymbol{\tau}_D : \mathbf{D}_A^p - \frac{\mathbf{q}}{\theta} \cdot \frac{\partial \theta}{\partial \mathbf{x}} \geq 0 \quad (44)$$

223 The first term represents the intrinsic dissipation and is non-negative by the flow rule. The last term is the
 224 dissipation due to heat conduction and is made non-negative by adopting Fourier's law: $\mathbf{q} = -k \frac{\partial \theta}{\partial \mathbf{x}}$, where
 225 the conductivity k is positive.

226 The heat equation is obtained by combining Equations (35) to (42), and the result comes out as

$$\rho_0 \bar{C}_v \dot{\theta} = \boldsymbol{\tau}_D : \mathbf{D}_A^p + \boldsymbol{\tau}_B : \mathbf{D} - \theta a_A \boldsymbol{\tau}_A : \mathbf{D}_A^e - \kappa_B [\ln(J) + 3\alpha\theta_0] \text{tr}(\mathbf{D}) + r - \text{div}(\mathbf{q}) \quad (45)$$

227 This evolution equation for the temperature includes contributions from thermoelastic heating, as in Miehe
 228 [47], and plastic dissipation in addition to the terms representing heat sources and heat conduction. By
 229 solving for the temperature rate, the heat equation is used to calculate the self-heating of the material.

230 3.2. Numerical integration

231 The governing equations of Part A of the constitutive model are compiled in Box 1.

Box 1: Governing equations of Part A.

$\boldsymbol{\sigma}_A = \frac{2}{J} \mu_A(\theta) \ln(\bar{\mathbf{V}}_A^e)$	elastic response
$\boldsymbol{\sigma}_D = \boldsymbol{\sigma}_A$	driving stress
$g(\boldsymbol{\sigma}_D) = \sqrt{\frac{3}{2} \boldsymbol{\sigma}'_D : \boldsymbol{\sigma}'_D} = \sigma_D^{\text{vm}} \geq 0$	plastic potential
$\mathbf{D}_A^p = \dot{p} \mathbf{N} = \mathbf{F}_A^e \dot{\mathbf{F}}_A^p \mathbf{F}_A^{-1}$	plastic rate-of-deformation
$\boldsymbol{\sigma}_V = \sum_{x=\alpha,\beta} \frac{k_B \theta}{V_x} \text{arsinh} \left(\frac{\dot{p}}{\dot{p}_{0,x}^*} \exp \left[\frac{\Delta H_x}{R\theta} \right] \right)$	viscous stress

232 A semi-implicit stress-update algorithm is used to integrate these equations in time, which implies that
 233 the direction of plastic flow \mathbf{N} and the absolute temperature θ lag one time step behind. Using the relation
 234 for the plastic rate-of-deformation tensor in Box 1, the inverse plastic deformation gradient is estimated by
 235 the relation

$$\left(\mathbf{F}_{A,n+1}^{p,i} \right)^{-1} = \left(\mathbf{1} - \Delta p_{n+1}^i \mathbf{F}_{n+1}^{-1} \mathbf{N}_n \mathbf{F}_{n+1} \right) \left(\mathbf{F}_{A,n}^p \right)^{-1} \quad (46)$$

236 where i denotes the current iteration in time step $n + 1$, $\Delta p_{n+1}^i = \dot{p}_{n+1}^i \Delta t_{n+1}$ is the equivalent plastic strain
 237 increment, and \mathbf{N}_n is the direction of plastic flow calculated from the previous time step, i.e.,

$$\mathbf{N}_n = \frac{3}{2} \frac{\boldsymbol{\sigma}'_{D,n}}{\sigma_{D,n}^{\text{vm}}} \quad (47)$$

238 The elastic deformation gradient is then calculated as

$$\mathbf{F}_{A,n+1}^{e,i} = \mathbf{F}_{n+1} \left(\mathbf{F}_{A,n+1}^{p,i} \right)^{-1} \quad (48)$$

239 which gives us the driving stress, $\sigma_{D,n+1}^i$ and the von Mises equivalent stress $\sigma_{D,n+1}^{vm,i}$, see Box 1. The
240 constitutive relations for the two dashpots give a residual function in the form

$$f(\dot{p}_{n+1}^i) = f_{n+1}^i = \sigma_{D,n+1}^{vm,i} - \sigma_{V,n+1}^i = 0 \quad (49)$$

241 where the viscous stress $\sigma_{V,n+1}^i$ is defined in Box 1. Using the secant method, an updated value of the
242 equivalent plastic strain rate is obtained by

$$\dot{p}_{n+1}^{i+1} = \dot{p}_{n+1}^i - f_{n+1}^i \frac{\dot{p}_{n+1}^i - \dot{p}_{n+1}^{i-1}}{f_{n+1}^i - f_{n+1}^{i-1}} \quad (50)$$

243 The iteration procedure continues until a convergence criterion is fulfilled. Note that the iterative scheme
244 is not self-started. In iteration $i = 1$ of the first increment the equivalent plastic strain rates \dot{p}_1^0 and \dot{p}_1^1 have
245 to be estimated, while in the remaining increments \dot{p}_n^1 is set equal to the converged value from the previous
246 increment \dot{p}_n , and \dot{p}_n^0 is kept constant and equal to \dot{p}_1^0 .

247 Concerning Part B of the rheological model, the stress tensor $\sigma_{B,n+1}$ is given explicitly by the deforma-
248 tion gradient \mathbf{F}_{n+1} and the temperature from the previous timestep θ_n , i.e.,

$$\sigma_{B,n+1} = \frac{\mu_B(\theta_n)\lambda_{\text{lock}}}{3\bar{\lambda}_{c,n+1}} \mathcal{L}^{-1} \left(\frac{\bar{\lambda}_{c,n+1}}{\lambda_{\text{lock}}} \right) \bar{\mathbf{B}}'_{n+1} + \kappa_B \ln(J_{n+1}) \mathbf{1} - 3\kappa_B \alpha(\theta_n - \theta_0) \mathbf{1} \quad (51)$$

249 Following the work of Miehe [37] and Sun et al. [38], the consistent tangent operator, \mathbf{C}^t , is found
250 by numerical differentiation. The deformation gradient is perturbed in such a way that only one of the six
251 unique components of the rate-of-deformation tensor is changed at the time, i.e.,

$$\Delta \mathbf{F}_{\pm}^{(kl)} = \pm \frac{\epsilon}{2} [(\mathbf{e}_k \otimes \mathbf{e}_l) \mathbf{F} + (\mathbf{e}_l \otimes \mathbf{e}_k) \mathbf{F}] \quad (52)$$

252 where ϵ is the perturbation coefficient set equal to 10^{-8} and \mathbf{e}_k for $k = 1, 2, 3$ are the Cartesian base vectors.
253 The perturbed deformation gradient, $\hat{\mathbf{F}}^{(kl)}$, is then obtained as

$$\hat{\mathbf{F}}_{\pm}^{(kl)} = \mathbf{F} + \Delta \mathbf{F}_{\pm}^{(kl)} \quad (53)$$

254 For each of the twelve deformation gradients thus obtained, the Cauchy stress tensor $\sigma(\hat{\mathbf{F}}^{(kl)})$ is calculated.
255 Using a central difference scheme, the consistent tangent operator \mathbf{C}^t is estimated as

$$C_{ij}^t = \frac{\sigma_{ij}(\hat{\mathbf{F}}_+^{(kl)}) - \sigma_{ij}(\hat{\mathbf{F}}_-^{(kl)})}{2\epsilon} \quad (54)$$

256 In Voigt notation this means that for each plus-minus perturbation of the deformation gradient, we obtain
 257 column (kl) in the 6×6 tangent operator $[\mathbf{C}^t]$ with row indices $ij = 11, 22, 33, 12, 13, 23$.

258 To ensure convergence, sub-stepping is used to limit the strain increment during the time step. The
 259 number of sub-steps, N , is controlled by the criterion

$$N = \max \left\{ \text{nint} \left[\frac{\Delta \varepsilon_{\text{eq}}}{\varepsilon_{\text{cr}}} + 0.5 \right], 1 \right\} \quad (55)$$

260 where nint is the *nearest integer* function, $\Delta \varepsilon_{\text{eq}} = \sqrt{\frac{2}{3} \Delta \boldsymbol{\varepsilon}' : \Delta \boldsymbol{\varepsilon}'}$ is the equivalent logarithmic strain incre-
 261 ment, $\Delta \boldsymbol{\varepsilon}' = \Delta \boldsymbol{\varepsilon} - \frac{1}{3} \text{tr}(\Delta \boldsymbol{\varepsilon}) \mathbf{1}$ is the deviatoric logarithmic strain increment tensor obtained by integrating the
 262 rate-of-deformation tensor \mathbf{D} over the time increment [50]

$$\Delta \boldsymbol{\varepsilon} = \int_{t_n}^{t_{n+1}} \mathbf{D} dt \quad (56)$$

263 Furthermore, ε_{cr} is a critical value set equal to strain-to-yield. If $N > 1$, new deformation gradients are
 264 calculated from the velocity gradient at the beginning of the time step, i.e.,

$$\mathbf{L}_n = \frac{\mathbf{F}_{n+1} - \mathbf{F}_n}{\Delta t_{n+1}} (\mathbf{F}_n)^{-1} \quad (57)$$

265 For sub-step number q , the deformation gradient, \mathbf{F}_q is then calculated as

$$\mathbf{F}_q = \left(\mathbf{1} + \frac{q \Delta t_{n+1}}{N} \mathbf{L}_n \right) \mathbf{F}_n \quad \text{for } q \in [1, N] \quad (58)$$

266 4. Material model calibration

267 Direct calibration from the experimental data was performed to obtain initial values of the parameters
 268 in the constitutive model. These initial values were then used in an optimization procedure, see Section 5.2.
 269 A brief review of the direct calibration procedure is given in the following.

270 4.1. Shear modulus

271 The shear modulus was estimated from already available experimental data given in Johnsen et al. [11].
 272 As shown in Figure 4, a clear strain rate and temperature dependence of the shear modulus was observed.
 273 This strain rate dependence of the shear modulus is, however, not incorporated in Equation (13). The
 274 material parameters in Equation (13) were found to be equal to $\mu_{A,\text{ref}} = 46$ MPa and $a_A = 0.03$ K⁻¹ from a
 275 least squares fit to the experimentally obtained shear moduli, see Figure 4.

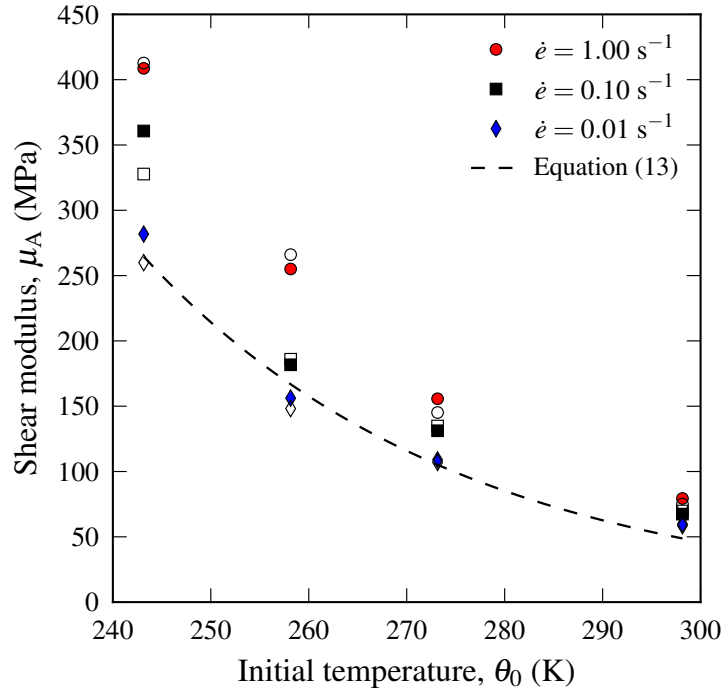


Figure 4: Temperature and strain rate dependence of the shear modulus of the material. Data adapted from [11].

276 4.2. Flow stress

277 The coefficients in the Ree-Eyring flow model [6] were identified from the stress-strain curves by using
 278 the flow stress, $\sigma_{0.15}$, at a fixed longitudinal strain magnitude of $\epsilon_L = 0.15$ for all investigated temperatures
 279 and strain rates. The least squares fit of Equation (17) to the experimental data is shown in Figure 5 along
 280 with the obtained parameters in Table 2. These six initial parameters were obtained from the twelve discrete
 281 experimental points in the space spanned by stress, strain rate and temperature using the Solver function in
 282 Excel. The material parameters obtained from the least squares fit have magnitudes that are comparable to
 similar parameters reported elsewhere in the literature, see e.g. [7, 51].

Table 2: Initial material parameters (before optimization) in the Ree-Eyring model, Equation (17).

V_α (nm^3)	$\dot{p}_{0,\alpha}$ (s^{-1})	ΔH_α (kJ/mol)	V_β (nm^3)	$\dot{p}_{0,\beta}$ (s^{-1})	ΔH_β (kJ/mol)
3.45	$1.38 \cdot 10^{28}$	188.6	3.10	$5.79 \cdot 10^{39}$	204.3

283

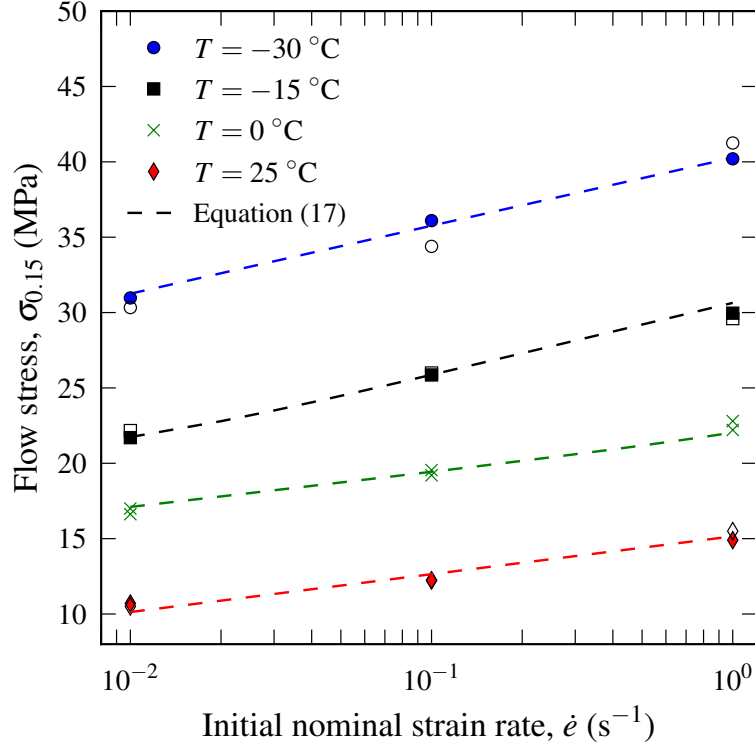


Figure 5: Temperature and strain rate dependence on the flow stress of the material. Data taken from [11].

284 4.3. Strain hardening

285 There are two contributions to strain hardening in the model: (1) orientational hardening σ_B in Part B
 286 capturing the effect of polymer chain alignment, and (2) isotropic hardening from the deformation dependent
 287 reference strain rates in the viscous dashpots in Part A.

288 The orientational hardening is modelled by the eight chain spring [5]. Simply put, the spring accounts
 289 for how the polymer chains align due to stretching and give rise to the abrupt change in strain hardening
 290 when approaching the locking stretch. To estimate the value of the reference shear modulus $\mu_{B,ref}$ and
 291 the locking stretch, λ_{lock} , a simple one-dimensional (1D) model was used. First we calculate the axial
 292 component of the stress from Equation (34) as

$$\sigma = \frac{\mu_B(\theta)\lambda_{lock}}{3J\bar{\lambda}_c} \mathcal{L}^{-1}\left(\frac{\bar{\lambda}_c}{\lambda_{lock}}\right) (\bar{\lambda}^2 - \bar{\lambda}_c^2) \quad (59)$$

293 where $J = \lambda^{1-2\nu}$, $\bar{\lambda}_c = \sqrt{\frac{1}{3}(\bar{\lambda}^2 + \frac{2}{\bar{\lambda}^{2\nu}})}$ and $\bar{\lambda} = J^{-1/3}\lambda$. Using a Poisson's ratio ν equal to 0.49, found from
 294 available experimental data in [11], and comparing the onset of strain hardening from Equation (59) with
 295 that from the experimental stress-strain curve at the reference temperature $\theta_{ref} = 298.15$ K, we find the
 296 values $\mu_{B,ref} = 2.0$ MPa and $\lambda_{lock} \approx 5.2$.

297 Next, the deformation dependent reference strain rates are found by fitting the expression for the viscous
 298 stress, σ_V in Equation (17), to the flow stress minus the stress contribution from Part B at different levels of
 299 deformation while keeping all parameters except the reference strain rate constant. From Figure 6 it is read-
 ily seen that there is a decrease in the reference strain rates as the deformation is increased. Equation (18) is

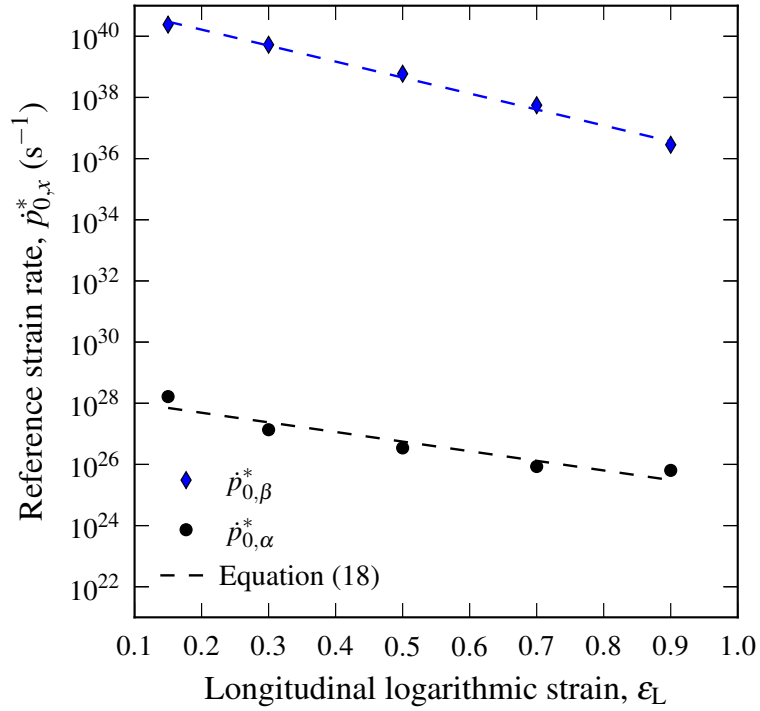


Figure 6: Reference strain rates, $\dot{p}_{0,x}^*$, as a function of longitudinal logarithmic strain.

300
 301 proposed to describe the deformation dependence of the reference strain rates $\dot{p}_{0,\alpha}^*$ and $\dot{p}_{0,\beta}^*$. A least squares
 302 fit of Equation (18) to the data in Figure 6 yielded: $b_\alpha = 7.2$ and $b_\beta = 12.0$.

303 5. Numerical model

304 5.1. Finite element model

305 All simulations were run in the commercial finite element program Abaqus/Standard, with the con-
 306 stitutive model implemented through a UMAT subroutine. Due to the symmetry of the tensile specimen
 307 and to save computational time, axisymmetric boundary conditions were employed in addition to one sym-
 308 metry plane, as indicated in Figure 7. Consequently, the transverse deformation anisotropy observed in
 309 the experimental tests is not included. Four-node axisymmetric elements with reduced integration and one
 310 thermal degree of freedom (CAX4RT) were used in all simulations with an element size of approximately

311 0.1 mm × 0.05 mm in the parallel part. Running on a standard workstation the analysis time ranged from
 312 approximately 2 to 12 minutes. Only a 1 mm portion of the grips was included in the model to reduce the

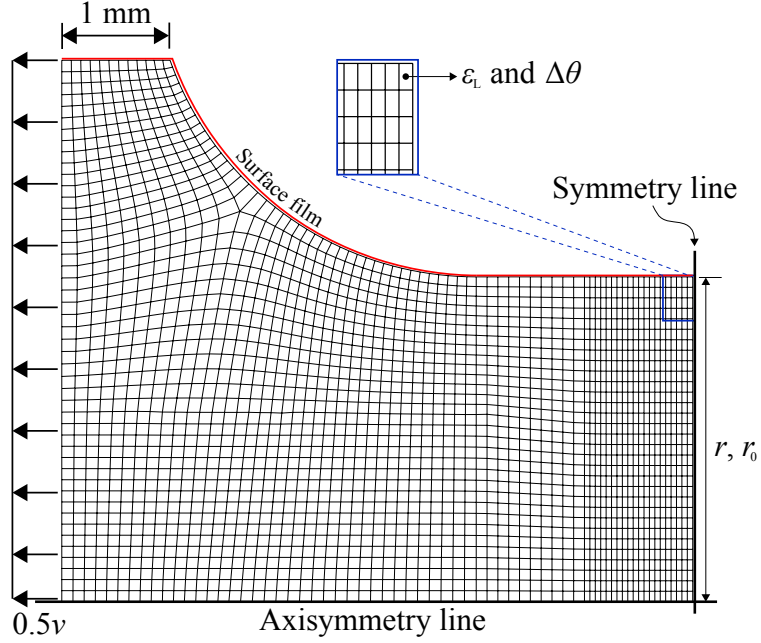


Figure 7: Axisymmetric finite element model with mesh and boundary conditions.

312
 313 computational time. The cross-head velocity, v , of the testing machine was applied as a velocity boundary
 314 condition at the positions indicated in Figure 7. Self-heating, $\Delta\theta$, and longitudinal strain, ε_L , were extracted
 315 from the indicated element in Figure 7, while the transverse strains were calculated as an average over the
 316 cross section at the symmetry line, i.e., $\varepsilon_1 = \varepsilon_2 = \ln(r/r_0)$, where r and r_0 are the current and initial radius
 317 of the parallel section, respectively. The Cauchy stress was then found as

$$\sigma = \frac{F}{A} = \frac{F}{\pi r^2} \quad (60)$$

318 where A is the current cross-sectional area, and F is the force extracted from the boundary conditions on
 319 the symmetry line.

320 In addition to the mechanical boundary conditions, a surface film was applied on the free surface of
 321 the tensile specimen, see the area highlighted with red in Figure 7. The surface film was used to simulate
 322 heat convection to air. Heat conduction within the material itself and heat convection to the surroundings
 323 were handled by the thermal solver in Abaqus. The values of the heat convection to air parameter, h_c ,
 324 the thermal conductivity, k , and the initial specific heat capacity, C_v , are given in Table 1. Lastly, the
 325 entire axisymmetric model was given an initial temperature equal to the surrounding temperature using the

326 predefined field feature in Abaqus/Standard.

327 5.2. Material parameters

328 The material parameters obtained in the Section 4 were used as initial values in a numerical optimization
 329 procedure where FE simulations of the tensile tests were run and the parameters varied manually to fit the
 330 experimental data. More specifically, the parameters related to the flow stress given in Eq. (17) and the bulk
 331 modulus κ_B were manually optimized. Since the initial parameters given in Table 2 for the viscous stress
 332 were obtained based on the initial nominal strain rate $\dot{\epsilon}$, the first step in the manual optimization procedure
 333 was to use the actual logarithmic strain rate $\dot{\epsilon}_L$ at the longitudinal strain magnitude where the flow stress
 334 was extracted. This procedure was repeated until yielding in the FE simulation was predicted at the correct
 335 stress magnitude. After a correct description of yielding was achieved, the parameters b_α and b_β governing
 336 the deformation dependence of the reference plastic strain rates $\dot{p}_{0,\alpha}$ and $\dot{p}_{0,\beta}$ were manually optimized to
 337 obtain a correct description of the strain hardening. Lastly, the volumetric strain obtained from simulation
 338 was compared with the experimental values to obtain an optimized value of the bulk modulus κ_B . The
 339 manual optimization was performed against the experimental results given in Figure 8 and 9. An alternative
 340 to this manual optimization procedure would have been to use an optimization software, e.g. LS-OPT. The
 341 material parameters used in the subsequent numerical simulations are presented in Table 3.

Table 3: Parameters in constitutive model.

Part A	$\mu_{A,\text{ref}}$	a_A	θ_{ref}	ΔH_α	V_α	$\dot{p}_{0,\alpha}$	b_α	ΔH_β	V_β	$\dot{p}_{0,\beta}$	b_β
	(MPa)	(K ⁻¹)	(K)	(kJ/mol)	(nm ³)	(s ⁻¹)	(-)	(kJ/mol)	(nm ³)	(s ⁻¹)	(-)
	46	0.028	298.15	179.5	4.72	$2.36 \cdot 10^{25}$	3.0	196.1	3.19	$6.13 \cdot 10^{36}$	10.0
Part B	$\mu_{B,\text{ref}}$	κ_B	λ_{lock}								
	(MPa)	(MPa)	(-)								
	2.0	1500	5.2								

342 6. Results and discussion

343 A comparison of the numerical results and the experimental results obtained by Johnsen et al. [11] are
 344 presented in the following. All numerical and experimental values were obtained from uniaxial tension

345 tests. Note that the results from the repeat tests presented in [11] are omitted, thus only the representative
346 experimental results are included in this study.

347 6.1. Stress-strain curves

348 Figure 8 presents the axial component of the Cauchy stress tensor as a function of the longitudinal
349 logarithmic strain from both simulations and experiments. Twelve configurations of temperature and strain
350 rate were investigated in total: four temperatures T of 25 °C, 0 °C, -15 °C and -30 °C and for each
351 temperature three nominal strain rates $\dot{\epsilon}$ of 0.01 s⁻¹, 0.1 s⁻¹ and 1.0 s⁻¹.

352 As shown in Figure 8, the overall behaviour of the material is well described by the constitutive model,
353 although the strain rate effect on Young's modulus (Figure 4) is not captured since viscoelasticity is not
354 incorporated. It appears from Figure 8 that the yield stress is accurately represented for all test configura-
355 tions by the incorporated Ree-Eyring [6] flow theory. Furthermore, we see that the strain hardening is well
356 described up to the onset of network hardening for all configurations except at room temperature. At room
357 temperature the onset of network hardening occurs too early in the simulations. However, as seen from
358 Figure 8, the onset of network hardening is continuously shifted to higher strain levels as the temperature
359 is decreased. This is caused by the constant locking stretch in combination with the reduced shear modulus
360 (Equation (28)) for decreasing temperatures in Part B of the constitutive model.

361 6.2. Volume change

362 The volumetric strain from the simulations was calculated using the longitudinal strain from the indi-
363 cated element in Figure 7 and the average transverse strain over the cross section, viz.

$$\varepsilon_V = \varepsilon_L + 2\varepsilon_1 = \varepsilon_L + 2 \ln\left(\frac{r}{r_0}\right) \quad (61)$$

364 Figure 9 compares the volumetric strain from simulations and experiments for all test configurations. Qual-
365 itative agreement between numerical predictions and experimental results is achieved at all investigated
366 temperatures.

367 In agreement with what is observed in experiments [11], reducing the initial temperature results in
368 more negative volumetric strain at moderate deformations in the numerical simulations. This is due to
369 the formation of a more prominent neck, causing the strain field to become more heterogeneous. The
370 heterogeneity of the strain field causes our method of calculating the volumetric strain, i.e., using the average
371 longitudinal and transverse strain over the cross section, to be less representative of the actual state inside

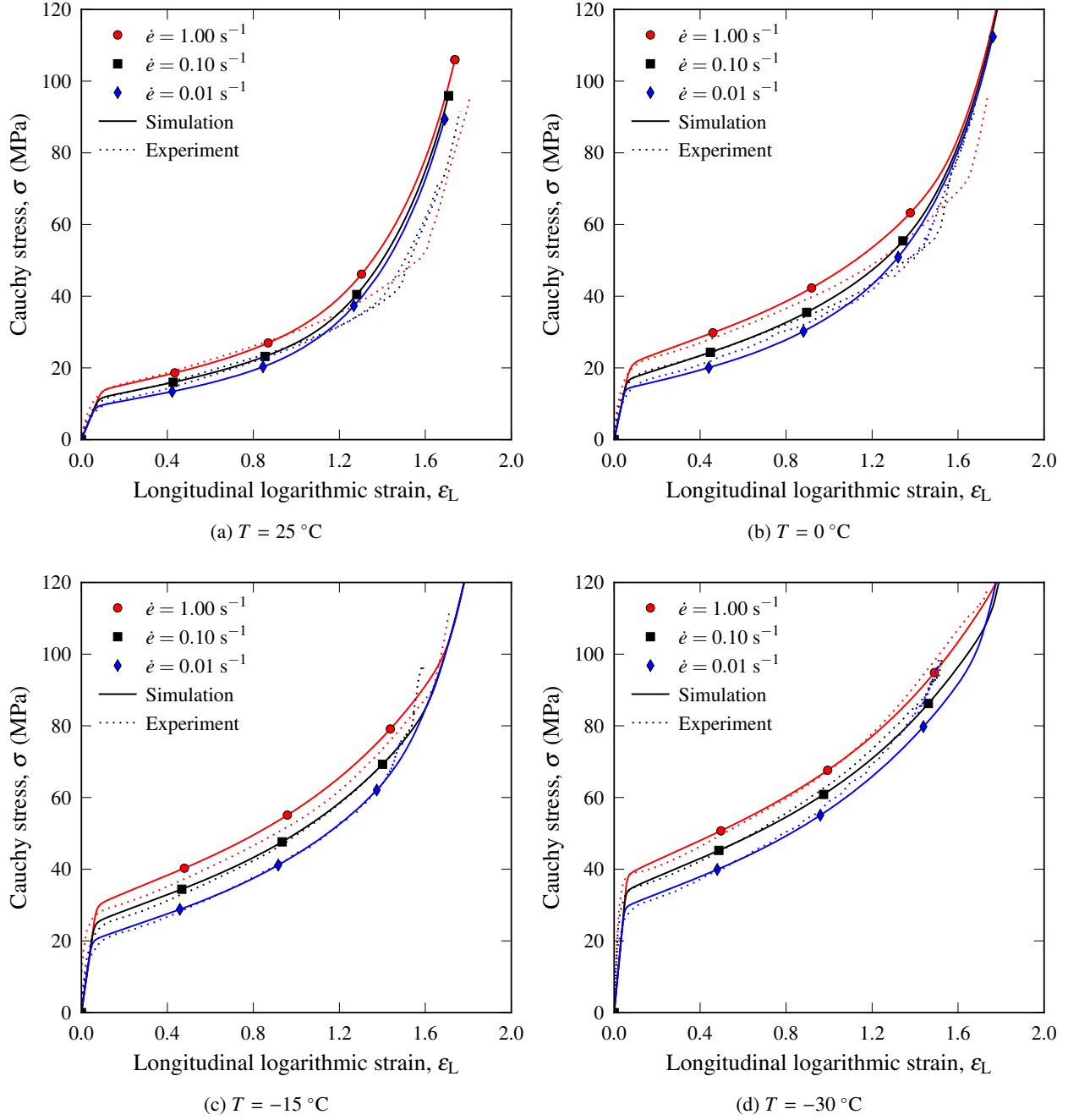


Figure 8: Cauchy stress vs. longitudinal logarithmic strain from uniaxial tension tests and numerical simulations at three different nominal strain rates, $\dot{\epsilon} = 0.01\text{ s}^{-1}$, $\dot{\epsilon} = 0.1\text{ s}^{-1}$, and $\dot{\epsilon} = 1.0\text{ s}^{-1}$, and at four different temperatures, (a) $T = 25^\circ\text{C}$, (b) $T = 0^\circ\text{C}$, (c) $T = -15^\circ\text{C}$ and (d) $T = -30^\circ\text{C}$.

372 the material, leading to the fictitious negative evolution of the volumetric strain in the beginning. A method
 373 to avoid this problem is to try estimating the heterogeneity of the strain field in the experiments, as proposed

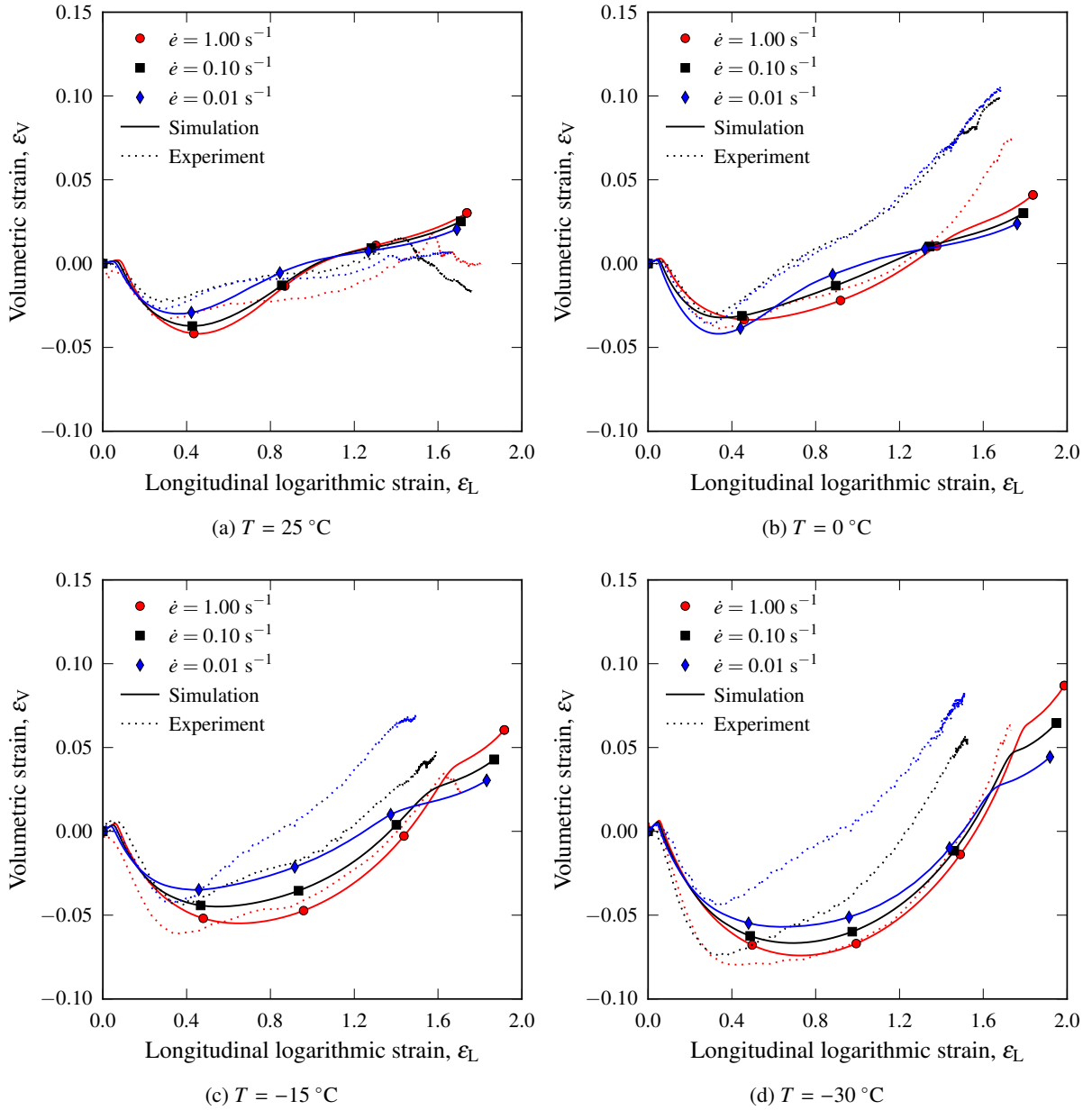


Figure 9: Volumetric strain vs. longitudinal logarithmic strain from uniaxial tension tests and numerical simulations at three different nominal strain rates, $\dot{\epsilon} = 0.01\text{ s}^{-1}$, $\dot{\epsilon} = 0.1\text{ s}^{-1}$, and $\dot{\epsilon} = 1.0\text{ s}^{-1}$, and at four different temperatures, (a) $T = 25^\circ\text{C}$, (b) $T = 0^\circ\text{C}$, (c) $T = -15^\circ\text{C}$ and (d) $T = -30^\circ\text{C}$.

374 by Andersen [52] and used by Johnsen et al. [31]. However, since the volumetric strain presented in Figure 9
 375 is calculated in a similar manner in experiments and simulations, this method was not further explored in
 376 this study. Furthermore, the contribution from thermal expansion to the volumetric strain can be estimated

377 by

$$\varepsilon_{V,\text{thermal}} = 3\alpha\Delta T \quad (62)$$

378 This contribution was estimated in Johnsen et al. [11] and was found to be small compared to the total
379 volumetric strain.

380 6.3. Self-heating

381 The temperature increment due to self-heating in the material is given as a function of longitudinal
382 logarithmic strain in Figure 10. Good qualitative agreement is found between simulations and experiments.
383 At small strains the model correctly describes the thermoelastic cooling effect. In the uniaxial tension tests
384 at the lowest strain rate, close to isothermal conditions are predicted. At the intermediate strain rate the
385 predicted temperature increment from simulations is in good agreement with experimental observations.
386 However, at the highest strain rate, the model does not generate enough heat. This is due to the interplay
387 between the elastic and plastic components of Part A, see Figure 3b. Since the elastic stiffness in Part A
388 is reduced for increasing temperature the consequence is a negative contribution to heat generation, which
389 has to be compensated by the plastic dissipation in the viscous dashpots and the entropic spring in Part
390 B. Furthermore, as the initial temperature decreases, the elastic stiffness increases, thus reducing elastic
391 deformation and in effect the elastic rate-of-deformation. This is the reason why the constitutive model
392 predicts a higher temperature increase as the initial temperature is lowered.

393 Another possible explanation for the observed discrepancies could be inaccuracies in the measured
394 heat on the surface of the specimen during testing, along with uncertainties in the experimentally obtained
395 thermal constants. The laser flash method [53] was used to obtain the specific heat capacity and the thermal
396 conductivity. Due to limitations in the testing apparatus, it was not possible to measure the parameters at
397 low temperatures. Consequently, the specific heat capacity and thermal conductivity were estimated at three
398 elevated temperatures of 25 °C, 35 °C and 50 °C. The thermal conductivity ($k = 0.56 \text{ W}/(\text{m}\cdot\text{K})$) was more
399 or less constant over the investigated temperatures with a standard deviation of $0.048 \text{ W}/(\text{m}\cdot\text{K})$, while the
400 specific heat capacity varied almost linearly with temperature, see Johnsen et al. [31]. However, the values
401 obtained at room temperature were used for both the specific heat capacity and the thermal conductivity in
402 the simulations.

403 The thermal camera used in the experiments by Johnsen et al. [11] was limited to temperatures above
404 -20 °C , as indicated by the dashed line in Figure 10d. It should also be mentioned that the jagged shape

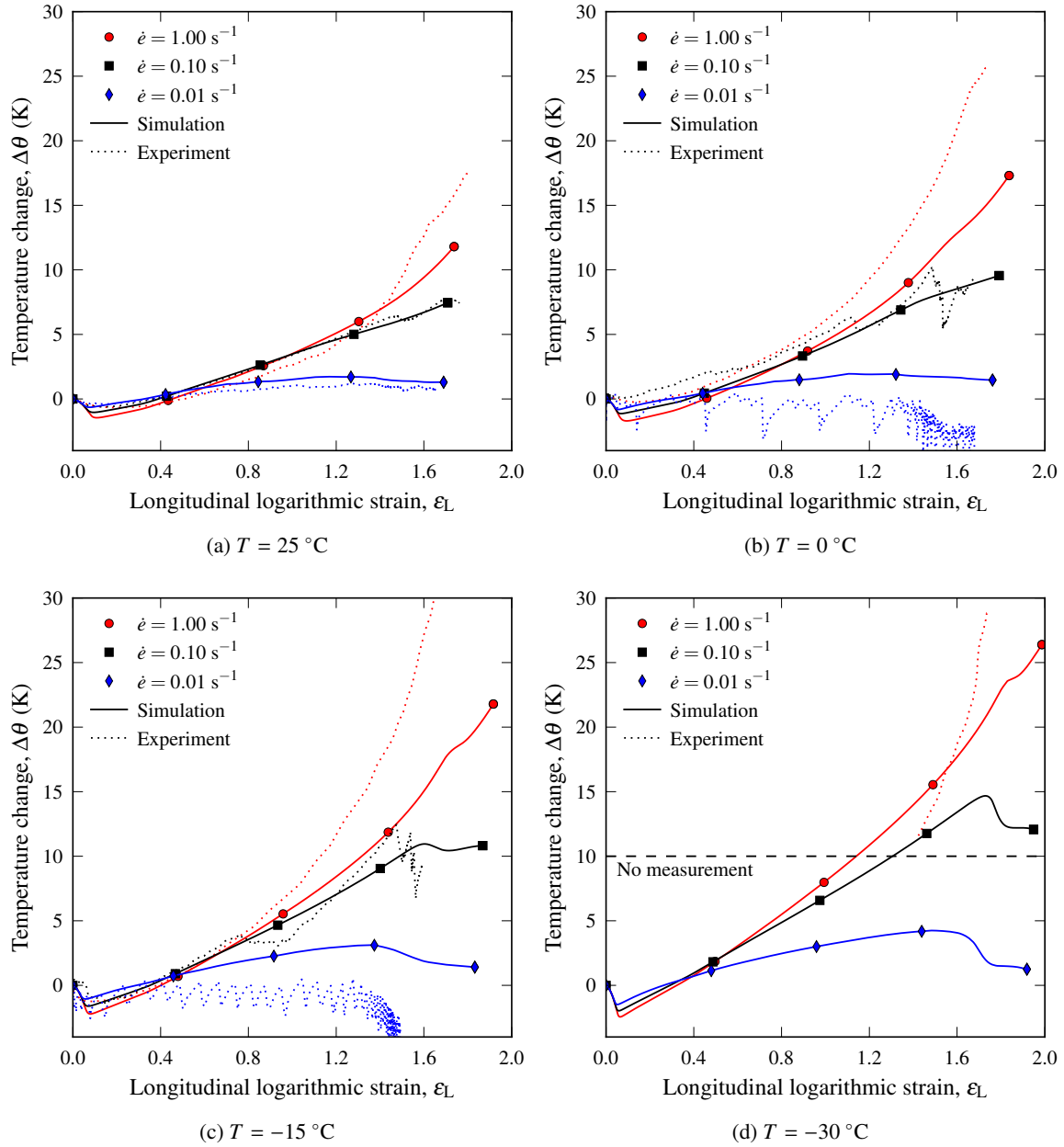


Figure 10: Temperature change vs. longitudinal logarithmic strain from uniaxial tension tests and numerical simulations at three different nominal strain rates, $\dot{\epsilon} = 0.01 \text{ s}^{-1}$, $\dot{\epsilon} = 0.1 \text{ s}^{-1}$, and $\dot{\epsilon} = 1.0 \text{ s}^{-1}$, and at four different temperatures, (a) $T = 25 \text{ }^\circ\text{C}$, (b) $T = 0 \text{ }^\circ\text{C}$, (c) $T = -15 \text{ }^\circ\text{C}$ and (d) $T = -30 \text{ }^\circ\text{C}$.

405 of the temperature increment vs. longitudinal strain curves at temperatures below $25 \text{ }^\circ\text{C}$ is caused by the
 406 influx of liquid nitrogen during the tension test.

407 6.4. Force-displacement curves

408 As a further validation incorporating the response of the entire tension test sample, force vs. displace-
409 ment curves are shown in Figure 11. The evolution of the force up to the peak value is well captured, along
410 with the subsequent force drop. In the simulations of the room temperature experiments, the force levels
411 are in general overestimated. This is attributed to a too high value of the shear modulus in Part B, in com-
412 bination with a too low value of the locking stretch, thus overestimating the strain hardening. For the tests
413 at 0 °C, good agreement is found between simulation and experiment for the two lowest strain rates. At the
414 highest strain rate there is not enough reduction in force after the peak force is reached, which for this con-
415 figuration is caused by the deformation dependent reference strain rates. For the two lowest temperatures,
416 a combination of the aforementioned effects is observed. At -30 °C the force reduction is overestimated
417 due to the reduced shear modulus in Part B ($\mu_B \approx \mu_{B,ref} \cdot \frac{243.15}{298.15} = 0.81\mu_{B,ref}$), while at -15 °C the force
418 in the simulation stabilizes earlier than in the experiment because of the isotropic hardening of the viscous
419 dashpots.

420 6.5. Strain rate

421 As shown in Figure 12, there is an overall good agreement between the strain rate from simulations,
422 extracted from the indicated element in Figure 7, and the strain rate from experiments. At room temperature
423 the strain rate in the simulations decreases too rapidly. This is due to strain hardening from Part B of the
424 model, which reduces the strain rate by propagating the neck too early. As seen from Figure 12, this effect is
425 continuously decreased as the initial temperature is reduced, which is caused by the reduced shear modulus
426 in Part B. The reduced shear modulus delays the onset of network hardening, which again allows for a more
427 prominent neck to form. This causes, or rather maintains, the strain rate for a longer period before the neck
428 starts to propagate causing the strain rate to decrease. Furthermore, when the neck is fully propagated, the
429 strain rate stops decreasing and a sudden increase in strain rate is observed in all experiments and in the
430 simulations at the two lowest temperatures. This is caused by the re-straining of the specimen which occurs
431 when the neck is fully propagated to the shoulders.

432 6.6. Strain-displacement curves

433 A comparison of the local strain in the most deformed section of the specimen vs. the global displace-
434 ment curves from simulations and experiments is given in Figure 13. The displacement in the finite element
435 model was extracted at the nodes where the velocity boundary condition was applied, see Figure 7.

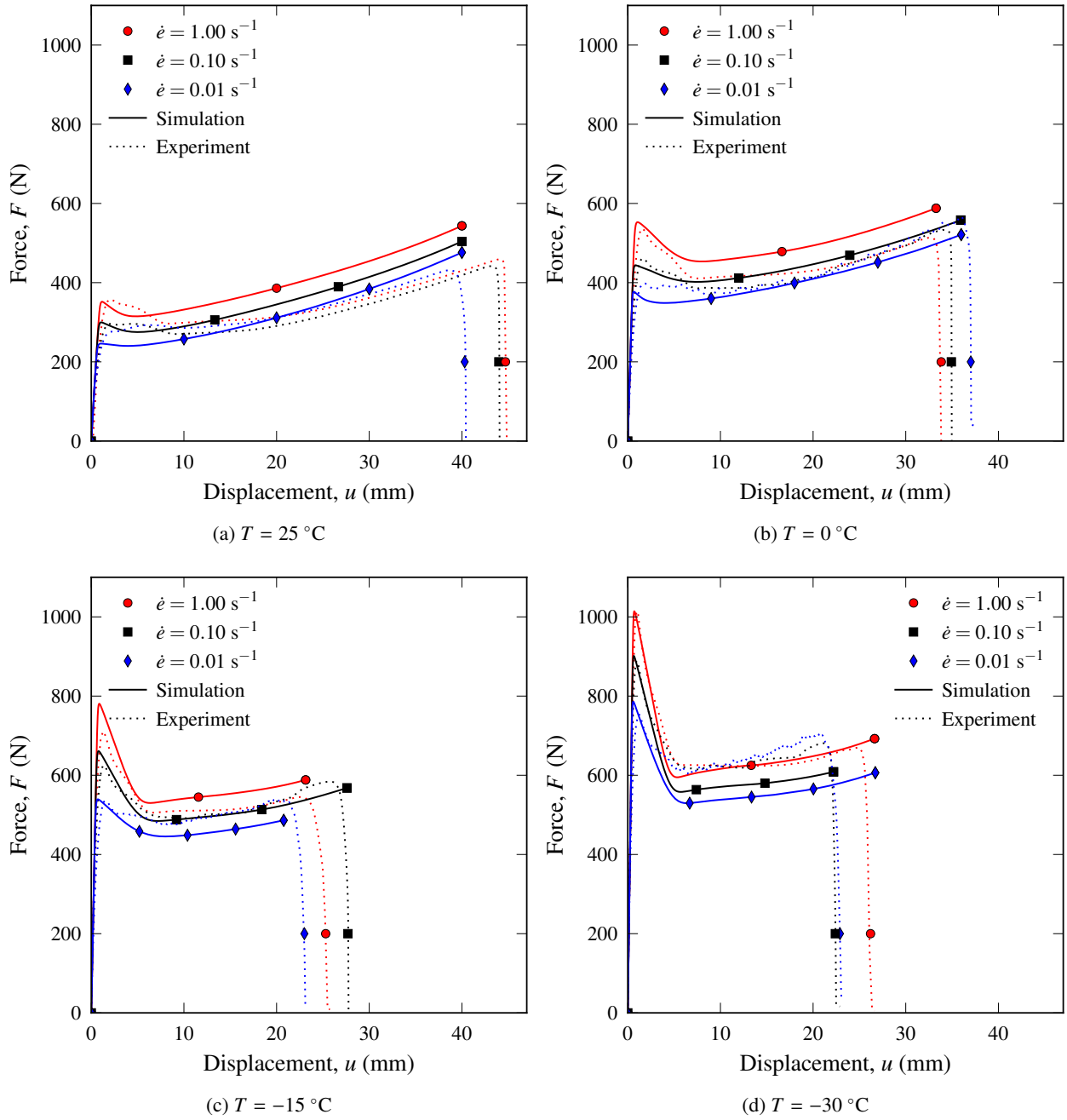


Figure 11: Force vs. displacement curves from uniaxial tension tests and numerical simulations at three different nominal strain rates, $\dot{\epsilon} = 0.01\text{ s}^{-1}$, $\dot{\epsilon} = 0.1\text{ s}^{-1}$, and $\dot{\epsilon} = 1.0\text{ s}^{-1}$, and at four different temperatures, (a) $T = 25\text{ }^{\circ}\text{C}$, (b) $T = 0\text{ }^{\circ}\text{C}$, (c) $T = -15\text{ }^{\circ}\text{C}$ and (d) $T = -30\text{ }^{\circ}\text{C}$.

436 Due to the constant locking stretch, the longitudinal strain saturates at approximately the correct level
 437 for all simulations. However, as has been the case for previous simulation results, the change in the shear

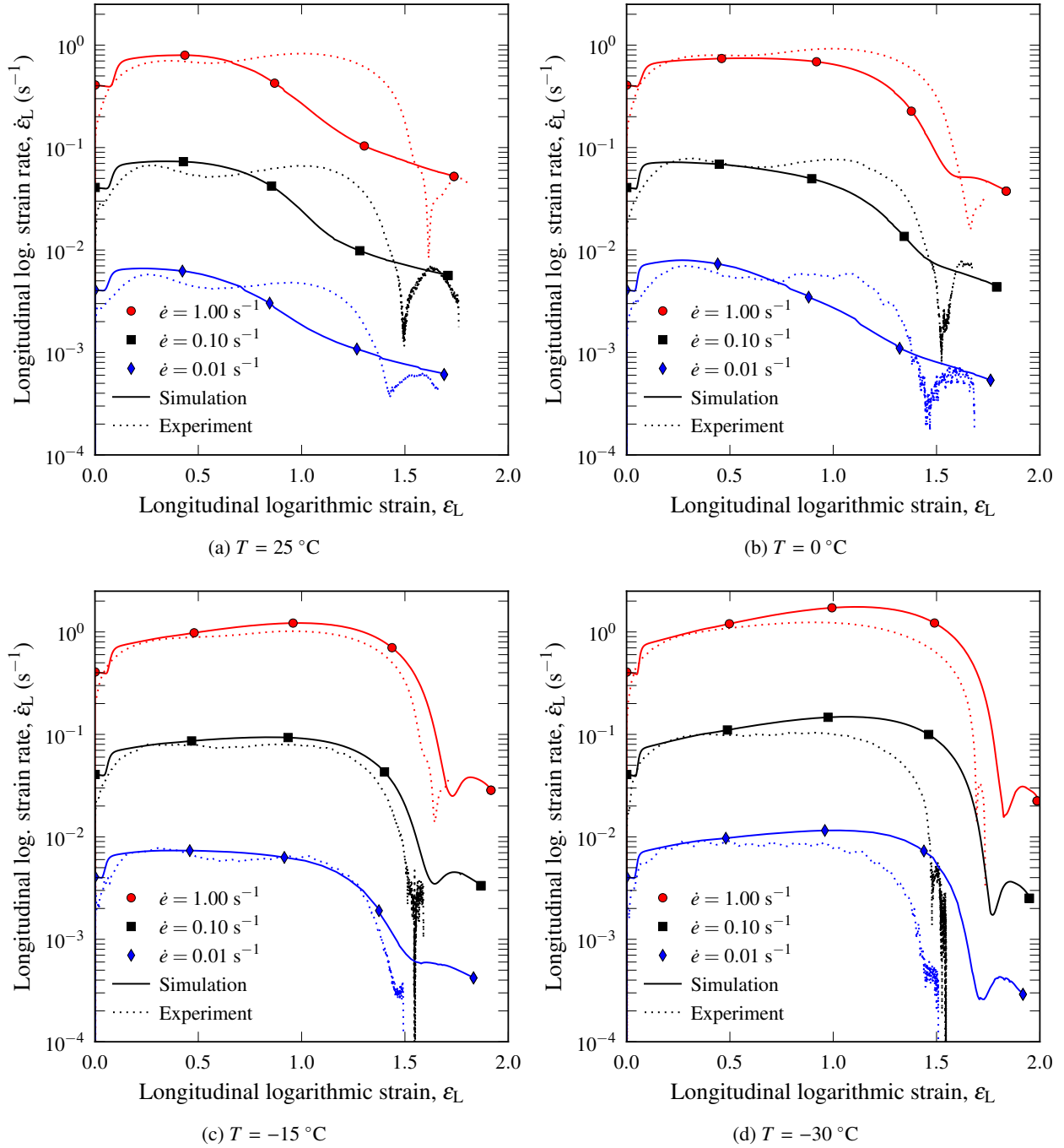


Figure 12: Longitudinal logarithmic strain rate vs. longitudinal logarithmic strain from uniaxial tension tests and numerical simulations at three different nominal strain rates, $\dot{\epsilon} = 0.01 \text{ s}^{-1}$, $\dot{\epsilon} = 0.1 \text{ s}^{-1}$, and $\dot{\epsilon} = 1.0 \text{ s}^{-1}$, and at four different temperatures, (a) $T = 25^\circ\text{C}$, (b) $T = 0^\circ\text{C}$, (c) $T = -15^\circ\text{C}$ and (d) $T = -30^\circ\text{C}$.

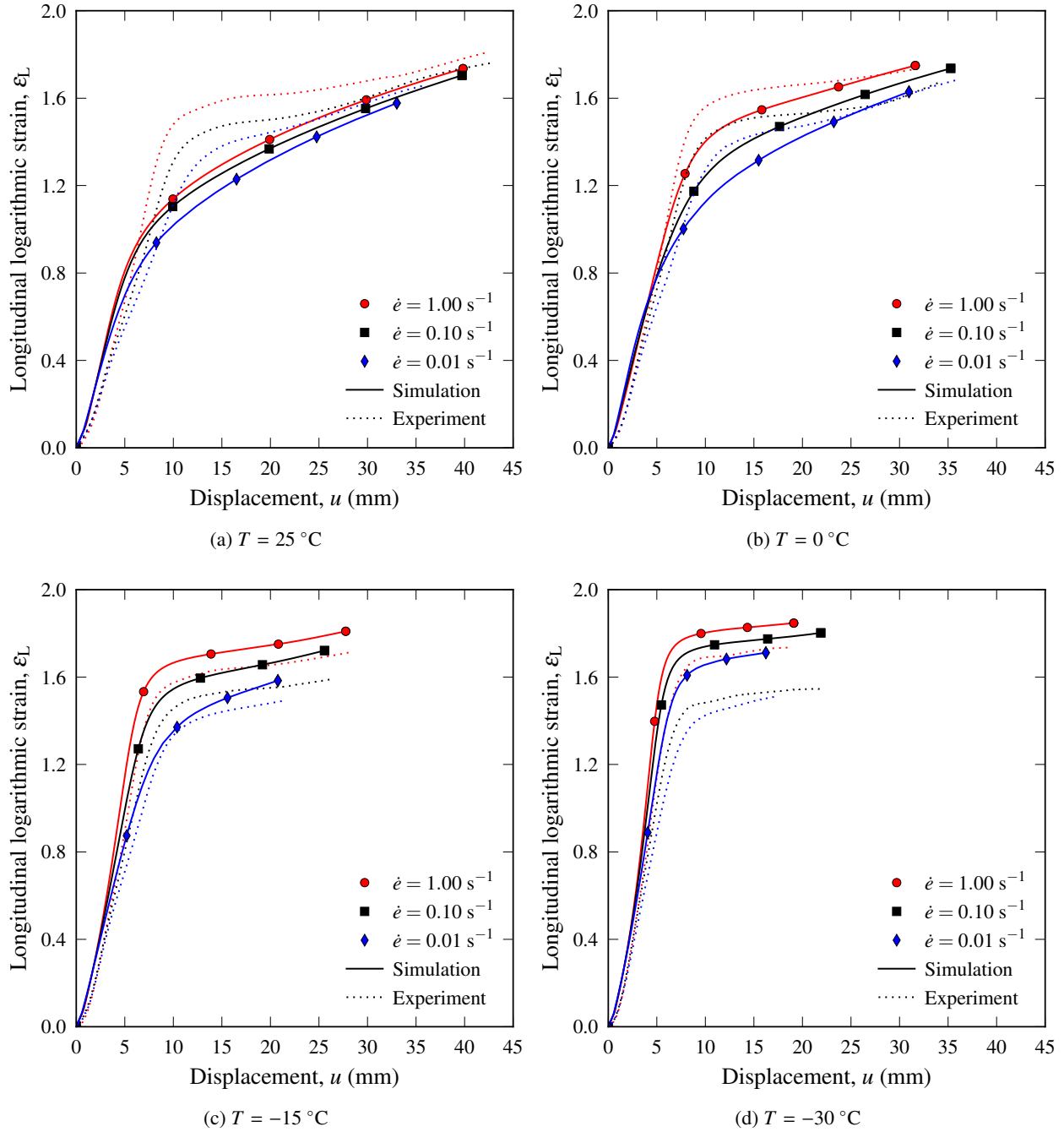


Figure 13: Local longitudinal logarithmic strain vs. global displacement from uniaxial tension tests and numerical simulations at three different nominal strain rates, $\dot{\epsilon} = 0.01 \text{ s}^{-1}$, $\dot{\epsilon} = 0.1 \text{ s}^{-1}$, and $\dot{\epsilon} = 1.0 \text{ s}^{-1}$, and at four different temperatures, (a) $T = 25 \text{ }^\circ\text{C}$, (b) $T = 0 \text{ }^\circ\text{C}$, (c) $T = -15 \text{ }^\circ\text{C}$ and (d) $T = -30 \text{ }^\circ\text{C}$.

438 modulus in Part B of the model is clearly evident. At room temperature, the strain saturates more gradually,
439 as seen in Figure 13a. As the temperature is decreased, the shear modulus in Part B is continuously reduced
440 leading to a rather accurate prediction of the longitudinal strain as a function of global displacement at
441 a temperature of $-15\text{ }^{\circ}\text{C}$ (Figure 13c). At a temperature of $-30\text{ }^{\circ}\text{C}$ (Figure 13d), the shear modulus has
442 been reduced too much, causing the longitudinal strain to saturate at a level which is too high. However,
443 it should be noted that the global displacement measured in the experiments is not directly comparable to
444 the displacement in the simulations. The reason for this is twofold: (1) the specimen was clamped in the
445 testing machine which might have caused some slippage between the clamping rig and the tensile specimen,
446 and (2) the finite machine stiffness might have affected the displacement recorded by the testing machine.
447 Nevertheless, Figure 13 demonstrates the constitutive model's capability of capturing both the local and
448 global material behaviour of the tensile specimen.

449 *6.7. Comparison of deformed shape*

450 Figure 14 shows a comparison between the deformed shape of the specimen from experiments and
451 simulations at room temperature and a strain rate of $\dot{\epsilon} = 1.0\text{ s}^{-1}$. The deformed shape of the finite ele-
452 ment model is outlined in red on the images from the experiments. As evident from Figure 14, there are
453 some discrepancies between simulation and experiment. At a relatively small displacement of $u = 3\text{ mm}$
454 (Figure 14a) the agreement between simulation and experiment is excellent. However, at a displacement
455 of 8 mm , the simulation deviates from experiment. The specimen has not contracted enough due to the
456 network hardening from Part B which limits the neck formation and accelerates neck propagation. All these
457 observations can be explained from Figure 13a where we see that at $u = 3\text{ mm}$ there is excellent agreement
458 between simulation and experiment. After $u \approx 6\text{ mm}$ the simulation starts to deviate from the experiment
459 due to the network hardening in Part B limiting the longitudinal strain, and a displacement of approximately
460 35 mm has to be reached before the longitudinal strains from simulation and experiment agree again.

461 **7. Concluding remarks**

462 We have presented a thermo-elasto-viscoplastic constitutive model describing the thermomechanical
463 behaviour of a cross-linked low density polyethylene (XLPE) at different temperatures and strain rates. The
464 constitutive model consists of two parts: Part A represents thermo-elasticity and thermo-viscoplasticity,
465 whereas Part B represents entropic strain hardening due to alignment of the polymer chains during defor-
466 mation. Assuming that the contributions from the main α and the secondary β relaxation processes are

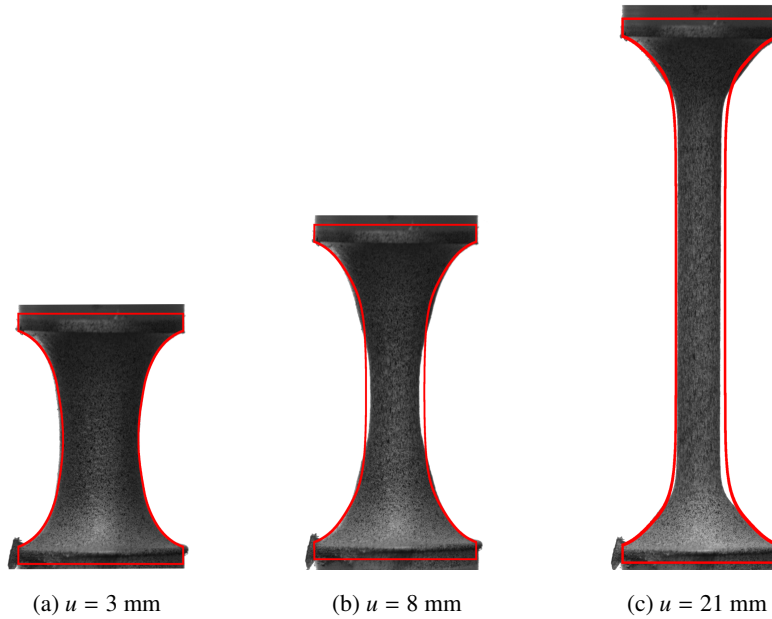


Figure 14: A comparison of the deformed shape of a specimen tested at $T = 25 \text{ }^\circ\text{C}$ and $\dot{\epsilon} = 1.0 \text{ s}^{-1}$ from finite element analysis and experiment at three magnitudes of displacement: (a) 3 mm, (b) 8 mm and (c) 21 mm. The deformed shape from the finite element analysis is outlined in red on the images from the experiment.

467 additive, Ree-Eyring dashpots were successfully used to describe yielding as a function of temperature
 468 and strain rate. The yield stress of the material was modelled as pressure insensitive, and the plastic flow
 469 was taken to be isochoric. There were two contributions to strain hardening in the model: (1) kinematic
 470 hardening from the eight chain spring in Part B, and (2) isotropic hardening introduced by the deformation
 471 dependent reference strain rates in the viscous dashpots. A phenomenological expression was proposed to
 472 describe the increase in Young's modulus as the material was cooled down. The constitutive model was im-
 473 plemented in a nonlinear finite element (FE) code using a semi-implicit stress update algorithm combined
 474 with sub-stepping and a numerical scheme to calculate the consistent tangent operator.

475 The constitutive model was calibrated from the stress-strain curves obtained in uniaxial tension tests
 476 performed at four different temperatures and three nominal strain rates, as reported in [11]. Considering
 477 the stress-strain curves, good agreement between simulations and experiments was achieved, as evident by
 478 Figure 8. Considering the increase in temperature, qualitative agreement was obtained between numerical
 479 predictions and experimental values. The predictions by the FE model in terms of volumetric strain, force
 480 vs. global displacement, local strain rate vs. local strain, global displacement vs. strain and the deformed
 481 shape of the tensile specimen were in good overall agreement with the experimental counterparts, and these

482 results serve as validation in the sense that the material model, which is calibrated from local stress-strain
483 data, is able to predict the global response adequately.

484 **Acknowledgements**

485 The authors wish to thank the Research Council of Norway for funding through the Petromaks 2 Pro-
486 gramme, Contract No.228513/E30. The financial support from ENI, Statoil, Lundin, Total, Scana Steel
487 Stavanger, JFE Steel Corporation, Posco, Kobe Steel, SSAB, Bredero Shaw, Borealis, Trelleborg, Nexans,
488 Aker Solutions, FMC Kongsberg Subsea, Marine Aluminium, Hydro and Sapa are also acknowledged. Spe-
489 cial thanks is given to Nexans Norway for providing the material. The help from Professor David Morin
490 and Dr. Torodd Berstad during the implementation of the constitutive model is also greatly appreciated. The
491 authors would also like to thank Professor Hans van Dommelen at Eindhoven University of Technology for
492 his insightful comments.

493 **References**

- 494 [1] R. Haward, G. Thackray, The use of a mathematical model to describe isothermal stress-strain curves in glassy thermoplastics,
495 Proceedings of the Royal Society of London 302 (1968) 453–472. doi:10.1098/rspa.1968.0029.
- 496 [2] H. Eyring, Viscosity, Plasticity, and Diffusion as Examples of Absolute Reaction Rates, The Journal of Chemical Physics 4
497 (1936) 283–291. doi:10.1063/1.1749836.
- 498 [3] L. R. G. Treloar, The Physics of Rubber Elasticity, 3rd Edition, Oxford University Press, Great Clarendon Street, Oxford,
499 1975.
- 500 [4] M. C. Boyce, D. M. Parks, A. S. Argon, Large inelastic deformation of glassy polymers. Part I: Rate dependent constitutive
501 model, Mechanics of Materials 7 (1988) 15–33. doi:10.1016/0167-6636(88)90003-8.
- 502 [5] E. M. Arruda, M. C. Boyce, A three-dimensional constitutive model for the large stretch behavior of rubber elastic materials,
503 Journal of the Mechanics and Physics of Solids 41 (1993) 389–412. doi:10.1016/0022-5096(93)90013-6.
- 504 [6] T. Ree, H. Eyring, Theory of non-Newtonian flow. I. Solid plastic system, Journal of Applied Physics 26 (1955) 793–800.
505 doi:10.1063/1.1722098.
- 506 [7] D. J. A. Senden, S. Krop, J. A. W. van Dommelen, L. E. Govaert, Rate- and temperature-dependent strain hardening of
507 polycarbonate, Journal of Polymer Science, Part B: Polymer Physics 50 (2012) 1680–1693. doi:10.1002/polb.23165.
- 508 [8] J. L. Halary, F. Laupretre, L. Monnerie, Polymer Materials: Macroscopic Properties and Molecular Interpretations, John
509 Wiley & Sons Inc, Hoboken, New Jersey, 2011, Ch. 1, p. 17.
- 510 [9] E. Arruda, M. Boyce, Evolution of plastic anisotropy in amorphous polymers during finite straining, International Journal of
511 Plasticity 9 (1993) 697–720. doi:10.1007/978-94-011-3644-0_112.

- 512 [10] J. S. Bergström, S. M. Kurtz, C. M. Rinnac, A. A. Edidin, Constitutive modeling of ultra-high molecular weight
513 polyethylene under large-deformation and cyclic loading conditions, *Biomaterials* 23 (2002) 2329–2343. doi:10.1016/
514 S0142-9612(01)00367-2.
- 515 [11] J. Johnsen, F. Grytten, O. S. Hopperstad, A. H. Clausen, Influence of strain rate and temperature on the mechanical behaviour
516 of rubber-modified polypropylene and cross-linked polyethylene, *Mechanics of Materials* 114 (2017) 40–56. doi:https:
517 //doi.org/10.1016/j.mechmat.2017.07.003.
- 518 [12] M. Ponçot, F. Addiego, A. Dahoun, True intrinsic mechanical behaviour of semi-crystalline and amorphous polymers: Influ-
519 ences of volume deformation and cavities shape, *International Journal of Plasticity* 40 (2013) 126–139. doi:10.1016/j.
520 ijplas.2012.07.007.
- 521 [13] E. M. Arruda, M. C. Boyce, R. Jayachandran, Effects of strain rate, temperature and thermomechanical coupling on the
522 finite strain deformation of glassy polymers, *Mechanics of Materials* 19 (1995) 193–212. doi:10.1016/0167-6636(94)
523 00034-E.
- 524 [14] R. S. Hoy, M. O. Robbins, Strain Hardening of Polymer Glasses: Effect of Entanglement Density, Temperature, and Rate,
525 *Journal of Polymer Science, Part B: Polymer Physics* 44 (2006) 3487–3500. doi:10.1002/polb.21012.
- 526 [15] L. E. Govaert, T. A. P. Engels, M. Wendlandt, T. A. Tervoort, U. W. Suter, Does the Strain Hardening Modulus of Glassy
527 Polymers Scale with the Flow Stress?, *Journal of Polymer Science Part B: Polymer physics* 46 (2008) 2475–2481. doi:
528 10.1002/polb.21579.
- 529 [16] M. Wendlandt, T. A. Tervoort, U. W. Suter, Non-linear, rate-dependent strain-hardening behavior of polymer glasses, *Polymer*
530 46 (2005) 11786–11797. doi:10.1016/j.polymer.2005.08.079.
- 531 [17] D. J. A. Senden, J. A. W. van Dommelen, L. E. Govaert, Strain Hardening and Its Relation to Bauschinger Effects in Oriented
532 Polymers, *Journal of Polymer Science Part B: Polymer Physics* 48 (2010) 1483–1494. doi:10.1002/polb.22056.
- 533 [18] G. W. Adams, R. J. Farris, Latent Energy of Deformation of Bisphenol A Polycarbonate, *Journal of Polymer Science Part B:*
534 *Polymer Physics* 26 (1988) 433–445. doi:10.1002/polb.1988.090260216.
- 535 [19] M. C. Boyce, E. L. Montagut, A. S. Argon, The effects of thermomechanical coupling on the cold drawing process of glassy
536 polymers, *Polymer Engineering & Science* 32 (1992) 1073–1085. doi:10.1002/pen.760321605.
- 537 [20] S. Hillmansen, S. Hobeika, R. N. Haward, P. S. Leevers, The Effect of Strain Rate, Temperature and Molecular Mass on the
538 Tensile Deformation of Polyethylene, *Polymer Engineering & Science* 40 (2) (2000) 481–489. doi:10.1002/pen.11180.
- 539 [21] S. Hillmansen, R. N. Haward, Adiabatic failure in polyethylene, *Polymer* 42 (22) (2001) 9301–9312. doi:10.1016/
540 S0032-3861(01)00447-5.
- 541 [22] J. Richeton, S. Ahzi, K. S. Vecchio, F. C. Jiang, A. Makradi, Modeling and validation of the large deformation inelastic
542 response of amorphous polymers over a wide range of temperatures and strain rates, *International Journal of Solids and*
543 *Structures* 44 (2007) 7938–7954. doi:10.1016/j.ijsolstr.2007.05.018.
- 544 [23] D. Garcia-Gonzalez, R. Zaera, A. Arias, A hyperelastic-thermoviscoplastic constitutive model for semi-crystalline polymers:
545 Application to PEEK under dynamic loading conditions, *International Journal of Plasticity* 88 (2017) 27–52. doi:10.1016/
546 j.ijplas.2016.09.011.
- 547 [24] M. Polanco-Loria, A. H. Clausen, T. Berstad, O. S. Hopperstad, Constitutive model for thermoplastics with structural appli-
548 cations, *International Journal of Impact Engineering* 37 (2010) 1207–1219. doi:10.1016/j.ijimpeng.2010.06.006.
- 549 [25] R. Raghava, R. M. Caddell, G. S. Y. Yeh, The macroscopic yield behaviour of polymers, *Journal of Materials Science* 8

- (1973) 225–232. doi:10.1007/BF00550671.
- [26] A. S. Ognedal, A. H. Clausen, M. Polanco-Loria, A. Benallal, B. Raka, O. S. Hopperstad, Experimental and numerical study on the behaviour of PVC and HDPE in biaxial tension, *Mechanics of Materials* 54 (2012) 18–31. doi:10.1016/j.mechmat.2012.05.010.
- [27] L. Anand, N. M. Ames, V. Srivastava, S. A. Chester, A thermo-mechanically coupled theory for large deformations of amorphous polymers. Part I: Formulation, *International Journal of Plasticity* 25 (2009) 1474–1494. doi:10.1016/j.ijplas.2008.11.004.
- [28] N. M. Ames, V. Srivastava, S. A. Chester, L. Anand, A thermo-mechanically coupled theory for large deformations of amorphous polymers. Part II: Applications, *International Journal of Plasticity* 25 (2009) 1495–1539. doi:10.1016/j.ijplas.2008.11.005.
- [29] A. Maurel-Pantel, E. Baquet, J. Bikard, J. L. Bouvard, N. Billon, A thermo-mechanical large deformation constitutive model for polymers based on material network description: Application to a semi-crystalline polyamide 66, *International Journal of Plasticity* 67 (2015) 102–126. doi:10.1016/j.ijplas.2014.10.004.
- [30] V. Srivastava, S. A. Chester, N. M. Ames, L. Anand, A thermo-mechanically-coupled large-deformation theory for amorphous polymers in a temperature range which spans their glass transition, *International Journal of Plasticity* 26 (2010) 1138–1182. doi:10.1016/j.ijplas.2010.01.004.
- [31] J. Johnsen, F. Grytten, O. S. Hopperstad, A. H. Clausen, Experimental set-up for determination of the large-strain tensile behaviour of polymers at low temperatures, *Polymer Testing* 53 (2016) 305–313. doi:10.1016/j.polymertesting.2016.06.011.
- [32] J. Richeton, S. Ahzi, K. Vecchio, F. Jiang, R. Adharapurapu, Influence of temperature and strain rate on the mechanical behavior of three amorphous polymers: Characterization and modeling of the compressive yield stress, *International Journal of Solids and Structures* 43 (2006) 2318–2335. doi:10.1016/j.ijsolstr.2005.06.040.
- [33] E. N. Brown, P. J. Rae, E. B. Orler, The influence of temperature and strain rate on the constitutive and damage responses of polychlorotrifluoroethylene (PCTFE, Kel-F 81), *Polymer* 47 (2006) 7506–7518. doi:10.1016/j.polymer.2006.08.032.
- [34] D. A. Şerban, G. Weber, L. Marşavina, V. V. Silberschmidt, W. Hufenbach, Tensile properties of semi-crystalline thermoplastic polymers: Effects of temperature and strain rates, *Polymer Testing* 32 (2013) 413–425. doi:10.1016/j.polymertesting.2012.12.002.
- [35] C. Bauwens-Crowet, The compression yield behaviour of polymethyl methacrylate over a wide range of temperatures and strain-rates, *Journal of Materials Science* 8 (1973) 968–979. doi:10.1007/BF00756628.
- [36] F. J. Zerilli, R. W. Armstrong, Application of Eyring’s thermal activation theory to constitutive equations for polymers, in: *AIP Conference Proceedings*, Vol. 505, AIP, 2000, pp. 531–534. doi:10.1063/1.1303530.
- [37] C. Miehe, Numerical computation of algorithmic (consistent) tangent moduli in large-strain computational inelasticity, *Computer Methods in Applied Mechanics and Engineering* 134 (1996) 223–240. doi:10.1016/0045-7825(96)01019-5.
- [38] W. Sun, E. L. Chaikof, M. E. Levenston, Numerical approximation of tangent moduli for finite element implementations of nonlinear hyperelastic material models., *Journal of Biomechanical Engineering* 130 (2008) 061003–1–061003–7. doi:10.1115/1.2979872.
- [39] Borlink LS4201S, <http://www.borealisgroup.com/en/polyolefins/products/Borlink/Borlink-LS4201S/>, accessed:2016-1116.

- 588 [40] W. D. Callister Jr., D. G. Rethwisch, *Materials Science and Engineering*, 8th Edition, John Wiley & Sons, Inc., 2011, Ch.
589 Appendix B, p. A19.
- 590 [41] E. H. Lee, Elastic-Plastic Deformation at Finite Strains, *Journal of Applied Mechanics* 36 (1969) 1. doi:10.1115/1.
591 3564580.
- 592 [42] E. de Souza Neto, D. Perić, D. Owen, *Computational Methods for Plasticity: Theory and Applications*, John Wiley & Sons,
593 Ltd., Chichester, West Sussex, 2008.
- 594 [43] G. A. Holzapfel, *Nonlinear Solid Mechanics*, John Wiley & Sons, Ltd., Chichester, West Sussex, 2000.
- 595 [44] M. E. Gurtin, L. Anand, The decomposition $F = F_e F_p$, material symmetry, and plastic irrotationality for solids that are
596 isotropic-viscoplastic or amorphous, *International Journal of Plasticity* 21 (2005) 1686–1719. doi:10.1016/j.ijplas.
597 2004.11.007.
- 598 [45] M. Boyce, G. Weber, D. Parks, On the kinematics of finite strain plasticity, *Journal of the Mechanics and Physics of Solids*
599 37 (5) (1989) 647–665. doi:10.1016/0022-5096(89)90033-1.
- 600 [46] J. F. Besseling, E. van der Giessen, *Mathematical Modelling of Inelastic Deformation*, Chapman and Hall, 1994.
- 601 [47] C. Miehe, Entropic thermoelasticity at finite strains. Aspects of the formulation and numerical implementation, *Computer*
602 *Methods in Applied Mechanics and Engineering* 120 (1995) 243–269. doi:10.1016/0045-7825(94)00057-T.
- 603 [48] L. Anand, A constitutive model for compressible elastomeric solids, *Computational Mechanics* 18 (1996) 339–355. doi:
604 10.1007/BF00376130.
- 605 [49] R. Jedynek, Approximation of the inverse Langevin function revisited, *Rheologica Acta* 54 (2015) 29–39. doi:10.1007/
606 s00397-014-0802-2.
- 607 [50] Dassault Systèmes, Providence Road, Rhode Island, ABAQUS 6.14 Documentation (2014).
- 608 [51] L. C. A. van Breemen, T. A. P. Engels, E. T. J. Klompen, D. J. A. Senden, L. E. Govaert, Rate- and temperature-dependent
609 strain softening in solid polymers, *Journal of Polymer Science, Part B: Polymer Physics* 50 (2012) 1757–1771. doi:10.
610 1002/polb.23199.
- 611 [52] M. Andersen, An experimental and numerical study of thermoplastics at large deformations, Ph.D. thesis, Norwegian Uni-
612 versity of Science and Technology, NTNU (2016).
- 613 [53] ISO22007-4:2008, *Plastics - Determination of thermal conductivity and thermal diffusivity - Part 4: Laser flash method*,
614 2008.